UNIVERSITY OF GOTHENBURG

DEPARTMENT OF PHYSICS

DEVELOPMENT OF A DEM-FEM FRAMEWORK FOR INFRASTRUCTURE SIMULATIONS

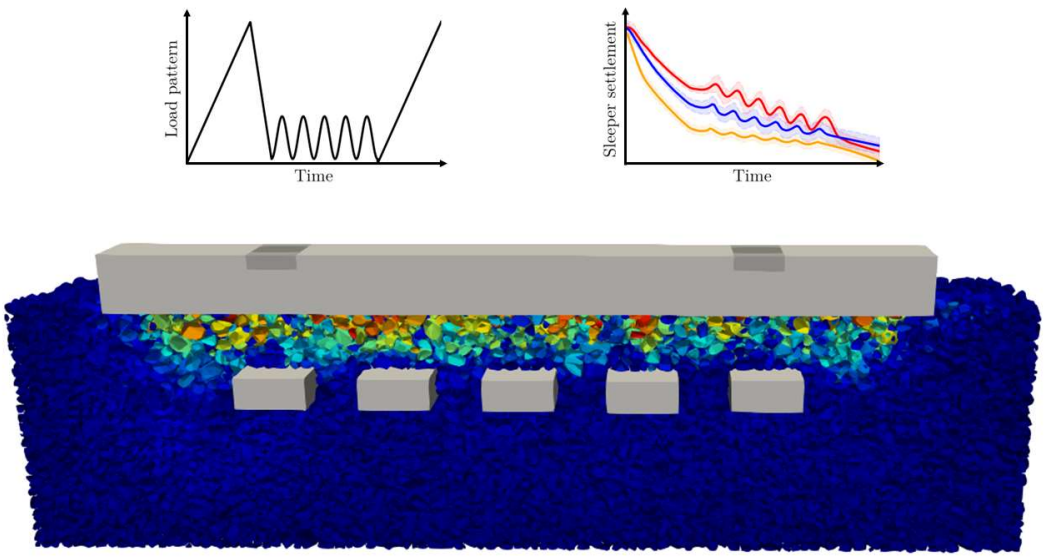

Anita Ullrich

Degree project for Master of Science (120 hec) with a major in Physics with Specialization in Complex Adaptive Systems
2022, 120 HEC
Second Cycle

Master's thesis 2022

Development of a DEM-FEM framework for infrastructure simulations

ANITA ULLRICH

UNIVERSITY OF GOTHENBURG

Department of Physics
Fraunhofer-Chalmers Centre
Gothenburg University
Gothenburg, Sweden 2022

Development of a DEM-FEM framework for infrastructure simulations
ANITA ULLRICH

Supervisor: Elin Solberg, Fraunhofer-Chalmers Centre
Klas Jareteg, Fraunhofer-Chalmers Centre
Christoffer Cromvik, Fraunhofer-Chalmers Centre
Examiner: Mohsen Mirkhalaf, Department of Physics

Master's Thesis 2022
Department of Physics
Fraunhofer-Chalmers Centre
Gothenburg University
SE-405 30 Gothenburg
Telephone +46 31 786 0000

Cover: Cross-sectional simulation snapshot of a DEM-FEM simulation of the interaction between a sleeper and a rock particle bed together with the load pattern applied on the sleeper and the resulting sleeper settlement as plots.

Typeset in LaTeX
Printed by Chalmers Reproservice
Gothenburg, Sweden 2022

Development of a DEM-FEM framework for infrastructure simulations
ANITA ULLRICH
Department of Physics
Fraunhofer-Chalmers Centre
Gothenburg University

Abstract

This thesis presents a coupling algorithm of the discrete element method (DEM) and finite element method (FEM). The algorithm formulates an explicit coupling of transient simulations of particle systems interacting with elastic bodies. To lay a foundation for the requirements in terms of stability and temporal and spatial resolution, the DEM and FEM methods are introduced. The coupling algorithm is implemented in a Python framework, using the FCC in-house solvers Demify® and LaStFEM. The combined tool is applied to three different main scenarios. As a first case, the solver exchange of forces between the DEM and FEM solver is verified using a fixed elastic beam simulation with uniform load, comparing the deflection under the load of particles to an analytical condition. Second, the dynamic accuracy and stability of the coupling method is proven on a simulation of a steel sheet deflection under the load of particles flowing on the elastic object. The simulations are compared to experimental results and show good agreement with a measured sheet deflection. Finally, the coupled solver is used to simulate the interaction between a timber sleeper and a rock particle ballast bed. The particles are in the third case represented by a polyhedron particle model. The system is studied for variations of both material properties as well as different simulation parameters. The coupled solver is shown to capture dynamic effects in the ballast bed under a dynamic load cycle. The simulation results are compared to experimental results of the pressure distribution in the bed from the open literature and demonstrate good qualitative and quantitative agreement with the experiments. The overall performance of the different parts of the solver is presented and it is shown that the developed tool is capable of simulating large scenarios with very good performance on desktop computers with a single GPU.

Keywords: Discrete element method, Finite element method, DEM-FEM coupling, railroad simulation, ballast material simulation.

Acknowledgements

First of all, I would like to express my appreciation of my supervisor Elin Solberg. You always had an open ear for my questions or discussions and helped me throughout the thesis to consider different points of view. Your input on the code development, the actual master thesis report and physics have been highly valuable. I want to thank my supervisor Klas Jareteg for support with the coupling development and my master thesis report. Your experience with particle simulations led to interesting discussions and helped me to gain a deeper understanding. I want to thank my supervisor Christoffer Cromvik for the supervision on finite element simulations and for the support with my master thesis report. Your expertise with finite elements and the physics behind have been very valuable throughout the thesis. I want to thank Johannes Quist. Your expertise with rock particle simulations led to numerous valuable discussions and insights. I want to thank the DEM team at FCC for great discussions and support. I want to acknowledge FCC in general, especially the head of the computational engineering department Fredrik Edelvik. Thank you for giving me the opportunity to write this master thesis about this interesting and important topic which builds a foundation for following projects. I want to thank the whole department for a great work environment and the interest in my work.
Furthermore, I want to thank my examiner Mohsen Mirkhalaf for his valuable feedback on my thesis.
I want to thank my family, in particular my parents and brothers for years of support throughout my studies and a never-ending interest in my daily work. Special thanks to Karl for encouraging and supporting me. I want to thank Linda and Lisa for your support, feedback on my report and encouragement.

This work has been supported in part by the Swedish Governmental Agency for Innovation Systems, VINNOVA, through the InfraSweden2030 program. The support is gratefully acknowledged.

Anita Ullrich, Gothenburg, June 2022

List of Acronyms

Below is the list of acronyms that have been used throughout this thesis listed in alphabetical order:

BVH	Bounding volumetric hierarchy
CAD	Computer-aided design
CPU	Central processing unit
CSV	Comma-separated values
CUDA	Compute unified device architecture
DEM	Discrete element method
FCC	Fraunhofer-Chalmers Centre
FEM	Finite element method
GPU	Graphics processing unit
H	Height
HMD	Hertz Mindlin Deresiewicz
L	Length
PDE	Partial differential equation
SEK	Swedish krona
STL	Standard triangulation language
W	Width

Notations

$x \coloneqq y$	x is defined as y
$\dot{x}$	Time derivative of x
$\ddot{x}$	Second time derivative of x
DEM theory	
$\mathbf{v}$	Translational velocity $[\frac{\mathrm{m}}{\mathrm{s}}]$
$\boldsymbol{\omega}$	Angular velocity $[\frac{1}{\mathrm{s}}]$
$\mathbf{F}^c$	Contact force [N]
$\mathbf{F}^g$	Gravitational force [N]
m	Mass [kg]
I	Moment of inertia $[\mathrm{kg} \cdot \mathrm{m}^2]$
$\mathbf{M}$	Torque [Nm]
$\mathbf{a}$	Acceleration $[\mathrm{m/s}^2]$
$\mathbf{F}_{net}$	Net force [N]
r_{ds}	Dilation radius [m]
E	Young's modulus [Pa]
G	Shear modulus [Pa]
ν	Poisson's ratio
$\mathbf{F}$	Force [N]
$F_{n,e}$	Elastic normal force [N]
$F_{n,d}$	Dissipative normal force [N]
F_n	Normal force [N]
$F_{t,e}$	Elastic tangential force [N]
F_t	Tangential force [N]
μ_s	Friction coefficient
θ	Angle of repose [°]
Φ	Mass flow rate [kg/s]
ρ_p	Particle density $[\mathrm{kg/m}^3]$

FEM theory

$\mathbf{K}$	Stiffness matrix
u	Displacement vector
$\mathbf{M}$	Mass matrix
$\boldsymbol{\varepsilon}$	Strain tensor
$\boldsymbol{\sigma}$	Stress tensor
n_d	Space dimension, usually $n_d = 3$ here
g, h	Prescribed boundary displacements
f	Point force boundary condition
$\mathbf{n}$	Normal vector
Ω	Domain
Γ	Boundary of Ω
$\mathbb{S}$	Solution space
$\mathbb{V}$	Variation space
v	Test function from $\mathbb{V}$
$a(.,.), (.,.), (.,.)_\Gamma$	Symmetric bilinear form
$\mathbf{e}$	Unit vector
N	Shape function
ρ_s	Density [kg/m^3]
$\mathbf{C}$	Damping matrix
α, β, γ	Bossak-Newmark damping parameters

Coupling theory

T	Triangle mesh
M^F	FEM object mesh
T^F	FEM surface triangle mesh
T^D	DEM triangle mesh
Δt^F	FEM timestep [s]
Δt^D	DEM timestep [s]
Δt^C	Coupling timestep [s]
$\mathbf{P}_T$	Position of nodes of triangle mesh T
$\mathbf{V}_T$	Velocity of nodes of triangle mesh T
$\mathbf{A}_T$	Acceleration of nodes of triangle mesh T
$\mathbf{F}_T$	Forces at nodes of triangle mesh T

Contents

List of Figures

List of Tables

List of Algorithms

1

Introduction

The railroad is a significant part of the transport system and the amount of train passengers in Sweden has approximately doubled since the 90's. Sweden aims to develop a climate neutral transport system until 2050, as elaborated by Tågoperatörerna [1]. A part of the plan is for instance the construction of new railroads that withstand the load of faster express trains. These new railroads are to be an addition to already existing ones such that the train traffic is separable by its speed. This would allow for more efficient and time dense train traffic. According to Tågoperatörerna [1], twice the amount of railroads can lead to four times more trains passing that section. However, construction and maintenance of railroad is cost and resource intensive. Tågoperatörerna [1] factors in 12.5 billion SEK (1.2 billion €) to execute the plans, including the construction of new railroads. Trafikverket [2] states that they are responsible for 14,000 km of railroad in Sweden and the operating and maintenance cost is circa 6 billion SEK per year. Above all, the construction and maintenance of railroad infrastructure is expensive.

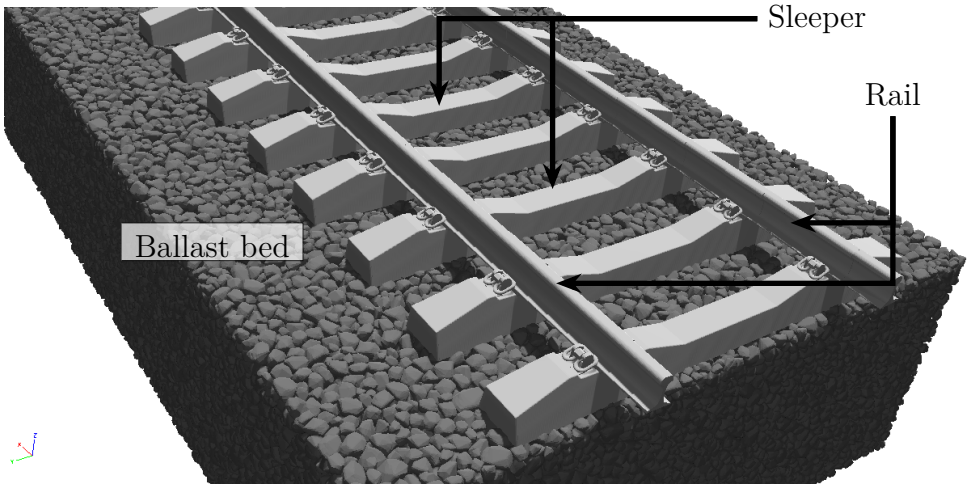

Figure 1.1: Visualization of a railroad system, including the ballast bed, the rails and the sleepers.

According to Naturvårdsverket [3], trains as a transport system only account for 0.3 % of the total traffic emissions and thus have the lowest emissions in Sweden. In contrast, automotive vehicles account for 92.6 %, shipping for 4.2 % and flights for 2.9 % of the total traffic emissions in Sweden in 2019. This emphasizes the importance of railroad for a sustainable infrastructure. To extend the railway network

and improve existing railways capital is needed. These expenses could be reduced with an optimized construction and maintenance.

In a ballast based railroad, the rails are clamped to sleepers which lie on a bed of ballast particles, typically crushed rocks or gravel. An illustration of the different components, including the nomenclature, is given in Figure 1.1. As the sleepers rest on the ballast bed, the ballast material is of key importance to provide reliable support for the sleepers, contribute to track stability and supply resilience and damping [4]. Thus, the characteristics of the ballast bed have great influence on the sleeper support and the ballast material is desired to be highly angular and have a high shear strength [5, 6]. However, the characteristics of ballast material change during its lifetime due to abrasion, which alters the mechanical characteristics of the ballast material [7] or causes the ballast particles to break [8]. This can possibly lead to settlement of the track [9]. Thus, regular ballast maintenance is needed, which is time and cost expensive [4]. A better understanding of the mechanical behavior of railroads, in particular the ballast bed, is key to better design and more efficient maintenance.

As railroad construction comes with a high cost in technical and financial resources, full-scale experimental setups are impractical. An alternative to experiments are simulations which typically approximate the behavior of objects, by solving physical equations numerically. A simulation framework of a railroad setup could offer the opportunity to investigate for instance altered construction methods and can be seen as a digital test bed to quickly try different variations in parameters as e.g. the size distribution of the ballast material. Various parameters could be tested and simulated faster and more cost efficiently than in real-world experiments.

The finite element method (FEM) is a simulation method to model structural objects and simulate deformations due to external loads. The discrete element method (DEM) is commonly used to simulate the dynamics of a large particle population. FEM is suitable to simulate the sleeper, whereas DEM can capture the mechanical properties of the ballast material consisting of individual rocks. In this thesis, we couple DEM and FEM to model the interaction of granular media with solid continua. Thus, we combine the strength of FEM to approximate the behavior of a sleeper with the strength of DEM in resolving the physics within the ballast bed to obtain a combined simulation method capturing the physics of the interaction between ballast bed and sleeper.

1.1 DEM-FEM coupling

For the purpose of simulating the interaction between sleeper and ballast, we develop a DEM-FEM coupling algorithm. In this section, we discuss the current state-of-art of such frameworks.

As a DEM-FEM coupling is applicable on different types of problems suggesting different coupling strategies, Stransky [10] suggested a classification of DEM-FEM coupling types as:

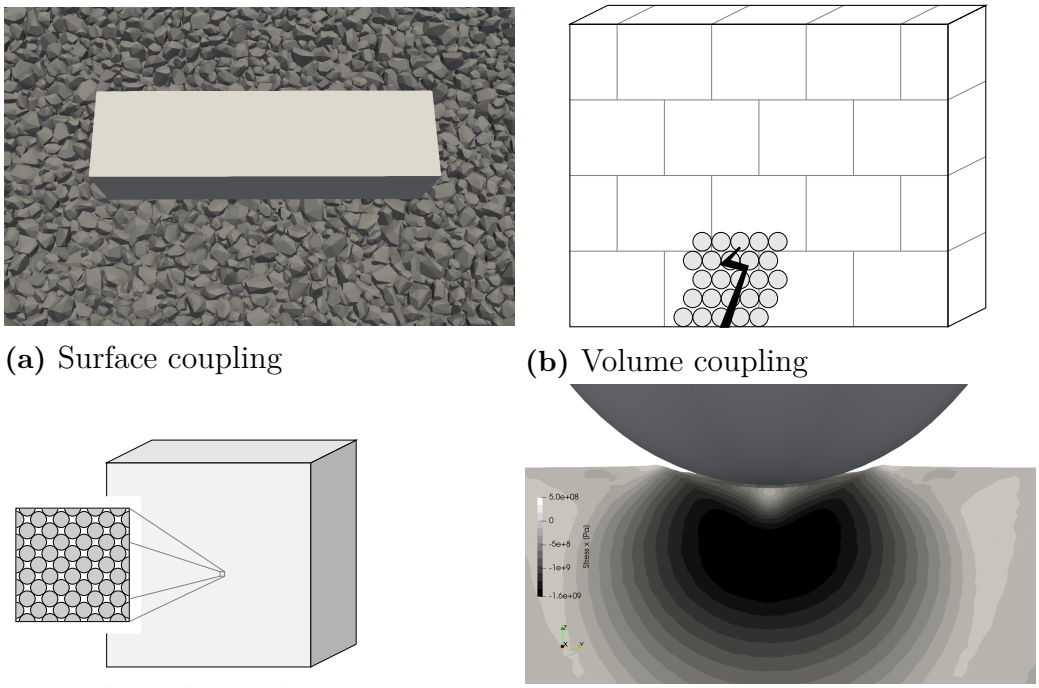

(a) Surface coupling

(b) Volume coupling

(c) Multi-scale coupling

(d) Contact coupling

Figure 1.2: Visualization of four different coupling types: Surface coupling (a), volume coupling (b), multi-scale coupling (c) and contact coupling (d).

- *Surface coupling* (Figure 1.2a), which simulates a granular medium interacting with a solid structure. The granular medium is simulated in the DEM domain and the solid structure in the FEM domain. A ballast-sleeper interaction exemplifies the surface coupling, as the ballast is purely modelled by DEM and the sleeper purely by FEM.
- *Volume coupling* (Figure 1.2b) which is used for instance to simulate fractures in solid structures. DEM and FEM model a shared structure. DEM is used to simulate the structure near a fracture and FEM simulates the intact parts. A brick wall is an example of a solid structure that can break. In case of a fracture, the bricks break and fall as individual elements out of the wall structure. Thus, the FEM object represents the wall in the example and DEM simulates the bricks near the fraction area including the ones falling out of the wall.
- *Multi-scale coupling* (Figure 1.2c), which simulates granular media under circumstances, where its properties on a macro-scale are similar to a continuum, e.g. sand. A box of sand consists of millions of particles, but on a large scale the sand can be seen as a continuous medium. Only when focusing on individual sand grains on a micro-scale perspective, the individual behavior is visible. In this case, FEM is used to model the macro-scale behavior of the medium and DEM models the micro-scale representing a detailed model of the macro-scale.

- *Contact coupling* (Figure 1.2d) is basically a pure FEM approach using the contact detection similar to DEM. An example of a contact coupling is shot peening where an object is shot on another object. The interaction physics become only relevant as soon as the one hits the other, resulting in a contact.

For the simulation of a ballast-sleeper interaction, the surface coupling is most suitable. Thus, within this thesis we focus on the surface coupling.

The field of possible applications of a coupled solution is wide, which is also represented by the wide range of different applications in the literature. A coupling method can generally be applied to any scenario of a solid structure interacting with a granular medium.

In the following, we give an overview of other applications in literature using a DEM-FEM surface coupling. Lu et al. [11] simulate particle dampers; Michael, Vogel, and Peters [12] simulate the interaction of a tire on sand, as also done by Nakashima and Oida [13] and Zeng et al. [14]; Zheng et al. [15] are concerned with simulating conveyor belt dynamics; Liang and Ji [16] model the reentry of a capsule; Chung et al. [17] investigate a granular sample under uni-axial compression.

Examples of a one-way coupling where only information is transferred from DEM to FEM are Tu et al. [18] with shot peening simulations and Liming et al. [19] who apply the coupling for the vibration of mining trucks based on particle damping.

Even though the multi-scale coupling is not considered further within this thesis, we state some interesting examples. Such are the investigation of borehole instability by Wu, Zhao, and Guo [20], modelling of roll compaction progresses by Mazor et al. [21] and the study of three-body friction behavior by Wang et al. [22].

Some articles present validation and verification cases for coupling simulations. The small validation case of a single sphere falling onto or rolling on a beam is presented by Onate et al. [23], Meijaard [24] and Xu and Zhao [25]. Dratt and Katterfeld [26] present a case for verification as well as a validation case with experimental measurements.

The classification of a simulation case into verification or validation is not obvious. Both cases presented by Dratt and Katterfeld [26] are further investigated in this thesis and discussed as validation and verification cases. With verification we intend to prove a correct functionality of the coupling algorithm implementation, i.e. the correct data transfer from DEM to FEM. Of course, the reverse data transfer from FEM to DEM is also part of verification, but not performed within the verification case of our choice. Thus, the later validation cases can also be interpreted as verification of the coupling data transfer. With validation we rather describe a successful comparison to experimental real-world data, which indicates that the here developed coupling framework delivers qualitatively satisfactory approximations of experimental results.

1.2 Simulation of railroad

The importance of models to understand the mechanical behavior within the railroad ballast, especially considering the interaction between sleeper and ballast, was dis-

cussed previously. In this section we give more insight into the existing modelling approaches for railroad with a focus on simulations using a DEM-FEM coupling framework.

According to Alabbasi and Hussein [4], many approaches with analytical models for understanding the macroscopic behavior of the railroad ballast exist. Yet, analytical models are limited and give no insight into the microscopic behavior.

Concerning numerical approaches, Alabbasi and Hussein [4] discuss the continuous FEM and the discrete DEM simulation approach. An example of a pure FEM simulation is Sysyn et al. [27], that investigate the settlement of railway with ballast voids. Due to the nature of FEM, it is a powerful tool to model the macroscopic ballast behavior under different loading conditions, but cannot provide an understanding of the microscopic level. An example of a pure DEM simulation is Jing et al. [28] who model the interaction between hanging sleepers and ballast. As every particle is simulated with DEM, quantities can be evaluated and visualized on a microscopic and a macroscopic level. However, DEM is limiting in a sense of computational cost and memory usage, especially when considering long simulation scenarios or the analysis of a full track under dynamic loading. The performance of DEM can be improved significantly by computing on the GPU as the simulation method is suitable for parallelization.

Similar approaches are given by Kaewunruen and Mirza [29] who model the interaction between railway and a bridge with a hybrid discrete - finite element simulation. Wang et al. [30] couple DEM and FEM as a multi-scale coupling to simulate high-speed railways. Song et al. [31] perform laboratory experiments to investigate the pressure distribution within the ballast bed under cyclic loading, as well as DEM-FEM coupling simulations with comparison to their laboratory results. We choose to replicate the experiments of Song et al. [31] within this thesis to apply the coupling framework on railroad as well as for validation that the coupling is applicable for railroad simulations.

More literature on laboratory experiments and measurements is given by Zhang et al. [8] for the settlement of sleeper and track and the breakage of the ballast material. Koike et al. [32] perform sleeper and track panel pullouts and investigate the lateral resistance of sleepers.

1.3 Computational software at FCC

The Fraunhofer-Chalmers Centre (FCC) for industrial mathematics has developed in-house simulation frameworks for DEM and FEM. The FEM solver LaStFEM is implemented in C++ with a Python interface and designed for structural analysis. The solver supports a range of material models for different discretization types. LaStFEM provides a computational engine in the software suite IPS and in the tolerance analysis software RD&T. LaStFEM is used for all FEM simulations within this thesis.

Moreover, an in-house state-of-art explicit DEM solver Demify® in C++ with a Python interface has been developed at FCC. The solver supports multiple particle

representations, including spheres, multispheres and convex, non-convex and dilated convex polyhedra. Demify® has been applied for large scale road infrastructure research as seen in Quist, Hunger, and Jareteg [33] and Quist et al. [34]. Demify® is used for all DEM simulations within this thesis.

Within this thesis we develop a coupling algorithm purely in Python using the interfaces of both solvers. No development of the solvers themselves is performed within this thesis.

1.4 Research questions

As a guidance to approach the task of developing a coupling algorithm with the existing software Demify® and LaStFEM for the application of railroad simulations, a set of research questions is formulated.

The first milestone in this thesis is the general development of a coupling framework between the DEM and FEM solver. Thus, a first set of research questions is:

- How to develop a DEM-FEM coupling matching the current state-of-art in the open literature?
- How is a stable and convergent scheme between the solvers formulated and implemented?
- What are the temporal and spatial resolutions required to achieve convergent solutions?
- What are the required algorithms to get sufficient performance in the coupling?

Once a functioning coupling algorithm is in place and validated, it is applied to railroad simulations. Therefore, two additional research questions arise and are investigated in this work:

- What questions concerning railroad ballast simulations with DEM-FEM couplings are not answered yet by the current state-of-art?
- Can the influence of the shape of the particle be quantitatively characterized to show the importance for ballast simulations and railroad construction?

In the open literature, examples of simulations of railroad with a DEM-FEM coupling are available. However, no one else coupled FEM and DEM with complex shaped particles, the cases found in literature are performed with spherical particles.

In addition, to our knowledge no work from the open literature actually measured and disclosed the performance of the DEM-FEM coupling. The overall performance of the coupled simulations are limited by the efficiency of the individual DEM and FEM solvers. Nevertheless, the efficiency of the coupling algorithm itself determines its practicality and applicability to large-scale simulation scenarios.

In relation to the dimension of railroad tracks, we simulate a smaller sub-system of a ballast bed and sufficiently short time periods. Simulations of larger railroad segments are possible, although not the primary focus of the current thesis. We are here concerned with a segment of a ballast bed with one sleeper.

1.5 Outline of the thesis

As the coupling framework is built upon a DEM and FEM solver, we first give an introduction to the theory behind both simulation methods in chapter 2. Then, we introduce the formulation of the surface coupling implementation in chapter 3. In chapter 4 we compare the simulation of a fixed beam under constant uniformly distributed load to the analytical condition. To validate the coupling formulation, we reconstruct the experiment for a steel sheet under a material flow of wheat grains in chapter 5 and compare to the experimental deflection results of the steel sheet. Then, we simulate the interaction between a sleeper and a rock particle ballast bed in chapter 6. Finally, we conclude our work in chapter 7 and discuss the research questions as well as possible future work.

2

Theoretical background of the DEM-FEM coupling

In section 2.1 the concept of the discrete element method is further described. As we do not only simulate with spherical particles, but also complex shaped particles, we introduce the dilated polyhedron particle model in subsection 2.1.1. Then, the contact model is explained in subsection 2.1.2 giving insight into the forces acting between particles. In subsection 2.1.3 and subsection 2.1.4 we discuss the concept of the angle of repose as well as mass flow rate that are two important calibration quantities for DEM. Finally, we discuss the Rayleigh timestep in subsection 2.1.5 that gives an upper bound of a suitable choice of a timestep.

We give an interlude on the finite element method in section 2.2. As within this thesis we are only concerned with FEM for elastic problems, we introduce terms of the elasticity theory in subsection 2.2.1. We summarize the deduction of the FEM equation system to solve for the static and dynamic case in subsection 2.2.2 and subsection 2.2.3, respectively. FEM meshes can be represented in different ways and a representation for thin elements chosen in this thesis is discussed in subsection 2.2.4. In subsection 2.2.5 we introduce the Bossak-Newmark damping that we apply later on in practical results to achieve a stable numerical simulation.

2.1 Discrete Element Method

The history of the discrete element method goes back to 1979 when the first open literature concerning DEM was published by Cundall and Strack [35] for the analysis of rock mechanic problems. DEM simulates the physics of individual discrete rigid objects with a fixed geometry over time. The particles modelled by the rigid objects are considered stiff bodies that do not deform under incoming forces, but only move as a whole in space. All particles are tracked and updated individually over time. The forces between objects and particles and between particles themselves are resolved and computed. The resulting forces then determine the movement of the particles. Following Zhu et al. [36], the governing equations of change for the translational and angular velocity, respectively $\mathbf{v}_i$ and $\boldsymbol{\omega}_i$, of particle i are

$$m_i \dot{\mathbf{v}}_i = \sum_j \mathbf{F}_{ij}^c + \mathbf{F}_i^g, \tag{2.1}$$

$$I_i \dot{\boldsymbol{\omega}}_i = \sum_j \mathbf{M}_{ij}, \tag{2.2}$$

with m_i and I_i mass and moment of inertia of particle i, $\mathbf{F}_{ij}^c$ and $\mathbf{M}_{ij}$ contact force and torque acting on particle i by particle or body j and $\mathbf{F}_i^g$ the gravitational force.

The given equations are solved by explicit integration in explicit DEM. Thus, the positions of the next timestep are based on the previous particle position and the acting forces at that timestep. In contrast, in implicit DEM the particle state of the next timestep is included in the computation of the equation of motion. Thus, implicit DEM accounts for a coupled contact network instead of solely the direct contacts [37]. This leads to an increased stability and a larger timestep can be used to solve the system [38]. However, to update the movement in implicit DEM a system of equations needs to be solved, which is computationally more expensive than solving two equations per particle as in explicit DEM. Another advantage of the explicit DEM is that the equations 2.1 and 2.2 can be solved for each particle independently and thus are suitable for GPU computing. The DEM method implemented in Demify® is explicit.

Equation 2.1 is based on Newton's second law, stating that the net force $\mathbf{F}_{net}$ has the following relation to a particle's mass m and acceleration $\mathbf{a}$:

$$\mathbf{F}_{net} = m\mathbf{a}. \tag{2.3}$$

The velocity and position of the particle are then derived by integrating Equation 2.3 once or twice, respectively. Analogously, the angular velocity and orientation of the particle is obtained by integrating Equation 2.2.

Algorithm 1 Pseudo-algorithm of a common explicit DEM.

```
1: Initialize particle population and objects.
2: while simulating do
3:     Detect particle-particle and particle-object contacts.
4:     Resolve and accumulate (contact) forces.
5:     Update particle states (position, velocity, orientation, angular velocity).
6: end while
7: Post-process and analyze results.
```

In Algorithm 1, a pseudo-algorithm stating the common steps in an explicit DEM simulation is given. Before simulating, a particle population needs to be initialized as well as the objects that the particles interact with. In each iteration of a DEM simulation the contact pairs must be detected. A contact pair can consist of two particles or a particle and an object. For these contact pairs we resolve and accumulate the contact forces as well as external forces such as gravity. After solving the equations for the acceleration of the particle (here equations 2.1 and 2.2), the particle states get updated. A particle state includes its position, velocity, orientation and angular velocity. The three steps of contact detection, force accumulation and state update are repeated until the desired simulation time is reached. Then, post-processing of the results is performed.

An efficient contact detection is required to narrow down the number of pairs that the contact forces are computed for. The contact detection within this thesis is

performed with a bounding volume hierarchy (also known as BVH). When the interaction pairs are identified, we can compute the contact forces as described in subsection 2.1.2.

Only pairs that are sufficiently close to each other are detected as a contact pair. This suggests that only particles and objects that are direct neighbors influence a specific particle. However, the movement of particles is affected not only by neighboring particles but also from particles far away through the propagation of disturbance waves [36]. By choosing a numerical timestep small enough it is assumed that the disturbance cannot propagate farther than to immediate neighbors. Thus, the detection of pairs that are close to each other delivers a sufficient approximation of the pairs influencing each other [35]. The upper bound of timesteps that fulfill this criteria is often referred to as the *critical timestep*. One example of an upper bound is given by the Rayleigh timestep as further described in subsection 2.1.5. Hence, in DEM only the interaction forces and torques between immediate neighbouring particles are resolved and timestep analyses are crucial to obtain correct simulation results.

Many applications of DEM are concerned with non-spherical particles, but more complex shaped ones as rocks, which can lead to better approximations of the mechanical characteristics of the particle population. Although the simulation of spheres is efficient and quite simple, their ideal shape may not capture the realistic behavior of non-spherical particles and can lead to oversimplification due to rotation. For instance, the spherical shape limits the capacity of the particles to model interlocking [39].

There are different methods to represent a particle with a more complex shape than spheres. Some of them are multi-sphere geometries [40], polyhedral geometries [41] or dilated polyhedral geometries [42]. In this thesis we are concerned with the last geometry type when simulating non-spherical particles. The formulation and the applied force models of the dilated polyhedra within this thesis are following the approach by Ji, Sun, and Yan [42] and a description is given in subsection 2.1.1.

2.1.1 Dilated polyhedra

Within our simulations we only consider dilated *convex* polyhedra. A polyhedron is defined by a triangle mesh consistent of nodes that are connected by edges which enclose triangular faces. A dilating sphere with radius r_{ds} is applied onto the polyhedron surface. In more detail, the center of the dilating sphere is swept over the surface of the polyhedron and the sphere merges with the existing mesh at each point. This is based on the classical concept of the Minkowski sum [43] as visualized in Figure 2.1:

$$A \oplus B = \{x + y \mid x \in A, y \in B\}, \tag{2.4}$$

for polyhedron A and sphere B. The resulting volume has a surface that describes the dilated polyhedron with dilation radius r_{ds}. Thus, the polyhedron is smoothed out with the sphere acting as a smoothing operator - similarly to a convolution

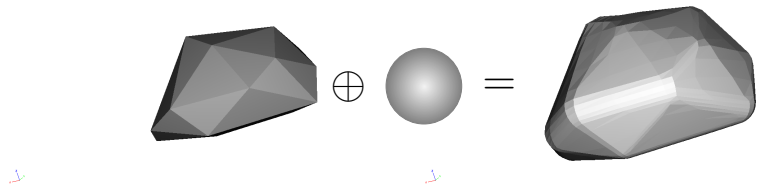

Figure 2.1: Visualization of the Minkowski sum concept for the case of a dilated polyhedron. On the left, a convex polyhedron rock model is shown. Together with the sphere displayed in the middle, a dilated polyhedron of the model results as shown on the right.

- resulting in the dilated polyhedron. The higher the dilation radius chosen, the smoother the dilated polyhedron gets.

The distance δ_{ij} between two dilated polyhedra i and j is then given as

$$\delta_{ij} = \Delta_{ij} - r_{ds,i} - r_{ds,j}, \tag{2.5}$$

with Δ_{ij} the distance between the two polyhedra corresponding to i and j and $r_{ds,i}, r_{ds,j}$ the dilation radii of the dilated polyhedra i and j.

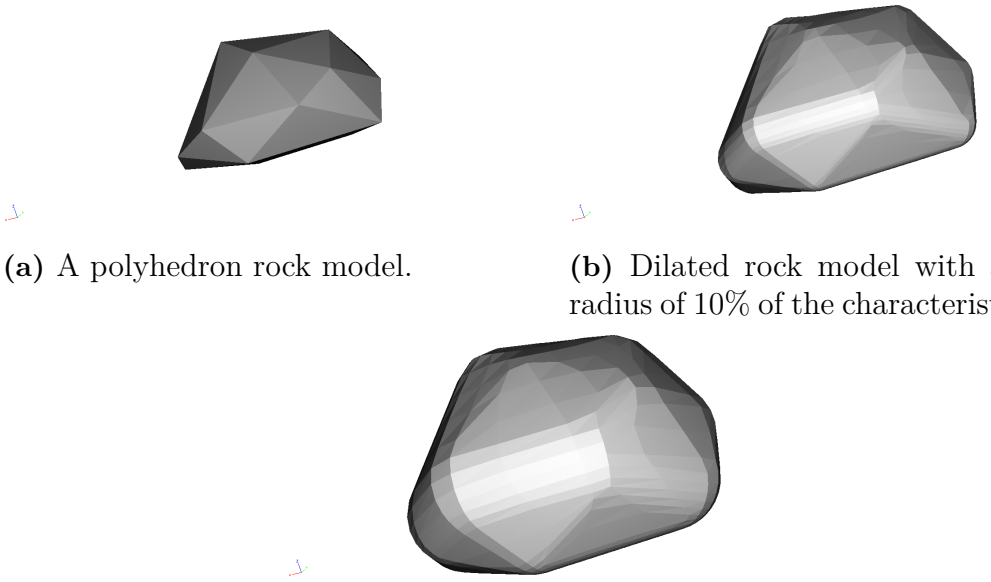

(a) A polyhedron rock model.

(b) Dilated rock model with a dilation radius of 10% of the characteristic length.

(c) Dilated rock model with a dilation radius of 20% of the characteristic length.

Figure 2.2: Visualization of a polyhedron (Figure 2.2a) representing a rock and its dilated version with different dilation radii of 10% (Figure 2.2b) and 20% (Figure 2.2c).

In Figure 2.2, a triangle mesh of a polyhedron representing a rock particle is visualized (see Figure 2.2a) together with two dilated models of the same polyhedron with different dilation radii. In Figure 2.2b, a dilation radius of 10% and in Figure 2.2c

a dilation radius of 20% is applied. The visualization demonstrates the effect of the dilation operator on the sharpness of edges or corners.

2.1.2 Contact model

When a particle gets close to another particle or object, their movement might result in a contact. Thereon, the contact is resolved in forces acting on the particles and determining their further movement. How exactly the forces are computed depends on the contact force model that is applied.

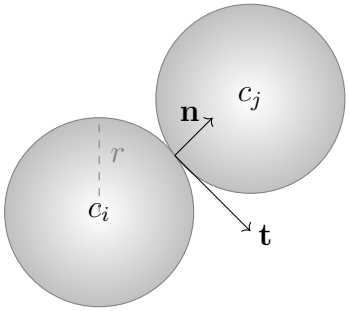

Figure 2.3: Visualization of a contact of two spheres with radius r together with the normal vector $\mathbf{n}$ and tangent vector $\mathbf{t}$ of the contact point. The centers of the two spheres are labelled as c_i and c_j.

A well-established model in DEM simulations is the theory of Hertz for the normal interaction and the theory of Mindlin and Deresiewicz for the tangential interaction, henceforth referred to as HMD model. The interaction can either be between two spheres or between a sphere and a planar surface. In this model, the contact is resolved into normal and tangential forces based on the normal and tangential direction of the contact point as visualized in Figure 2.3.

As it is a common model, there are also many variants of the HMD model. For modeling spheres we only consider the HMD model as it is stated in Thornton, Cummins, and Cleary [44], which we recap in the following. First of all, we introduce the normal elastic force that corresponds to the Hertz contact law [45] for elastic spheres. Then, we elaborate the computation of the dissipative normal force, that adds a damping term, as we consider inelastic spheres. In the case of elastic spheres, the dissipative normal force would be zero, as in Thornton, Cummins, and Cleary [46]. Finally, we follow the no-slip theory of Mindlin [47] to compute the tangential force.

Let $E_i, G_i, \nu_i, R_i, c_i$ be, respectively, the Young's modulus, shear modulus, Poisson's ratio, radius and center of sphere i. Having two spheres interacting with each other, labelled sphere i and j, the HMD model is assembled as follows.

The elastic normal force $F_{n,e}$ of the interaction is

$$F_{n,e} = \frac{4}{3} E^* R^{1/2} \delta^{3/2}, \tag{2.6}$$

where the effective modulus E^* is given by

$$\frac{1}{E^*} = \frac{1-\nu_i^2}{E_i} + \frac{1-\nu_j^2}{E_j} \tag{2.7}$$

and the effective radius R is computed as

$$R = \frac{R_i R_j}{R_i + R_j}. \tag{2.8}$$

Given the centers and radii, the indentation depth δ for sphere-sphere contacts is given as

$$\delta = \begin{cases} R_i + R_j - |c_j - c_i| & \text{if } |c_j - c_i| < R_i + R_j, \\ 0 & \text{otherwise.} \end{cases} \tag{2.9}$$

Moreover, the dissipative normal force $F_{n,d}$ is given as

$$F_{n,d} = 2\gamma\sqrt{m^* k_n} v_n, \tag{2.10}$$

where γ is the damping coefficient, m^* is the effective mass of the particles, k_n is the normal spring stiffness and v_n is the relative velocity in normal direction. The effective mass is computed as

$$m^* = \frac{m_i m_j}{m_i + m_j}, \tag{2.11}$$

where m_i, m_j are the masses of the two spheres. The normal spring stiffness is computed as

$$k_n = 2E^*\sqrt{R\delta}. \tag{2.12}$$

The total normal force F_n is then assembled as

$$F_n = F_{n,e} + F_{n,d}. \tag{2.13}$$

The achieved normal force is the force of the current timestep n which we now denote as F_n^n and thus we can compute the normal force increment as

$$\Delta F_n = F_n^n - F_n^{n-1}, \tag{2.14}$$

that is required to compute the tangential force.

Finally, let us state the computation of the tangential force. The elastic tangential force $F_{t,e}$ for timestep n is computed as

$$F_{t,e}^n = \begin{cases} F_{t,e}^{n-1} + k_t^n \Delta\delta & \text{if } \Delta F_n \geq 0, \\ F_{t,e}^{n-1} \left(\frac{k_t^n}{k_t^{n-1}}\right) + k_t^n \Delta\delta & \text{otherwise,} \end{cases} \tag{2.15}$$

where k_t is the tangential spring stiffness given as

$$k_t = 8G^* \sqrt{R\delta}. \tag{2.16}$$

The effective shear modulus G^* is computed as

$$\frac{1}{G^*} = \frac{1-\nu_i^2}{G_i} + \frac{1-\nu_j^2}{G_j}. \tag{2.17}$$

Thus, the tangential force takes the form

$$F_t = \begin{cases} F_{t,e}^n + 2\mu\sqrt{mk_t}v_t & \text{if } F_t < \mu F_n, \\ \mu F_n & \text{otherwise,} \end{cases} \tag{2.18}$$

where μ is the friction coefficient of the interaction. For a sphere-sphere interaction μ is referred to as Coulomb friction.

Having specified the normal and tangential force of the contact model, they can be added to the equation of change for the translational velocity (see Equation 2.1), as

$$\mathbf{F}_{ij}^c = F_n + F_t. \tag{2.19}$$

As motivated in subsection 2.1.1, we use complex shapes in the form of dilated polyhedra at a later stage of our simulations. For these, we use a modified Hertz-Mindlin contact model as it is stated by Ji, Sun, and Yan [42].

The normal contact force in this case takes the form

$$F_n = \frac{2\sqrt{2}G}{3(1-\nu)} {r_{ds}}^{1/2} \delta_d^{3/2}, \tag{2.20}$$

where r_{ds} is the dilation radius and δ_d is the overlap vector of the two interacting particles. The tangential force at timestep n, then takes the form

$$F_t^n = F_t^{n-1} - k_t \Delta t (\mathbf{v}_{ij} - \mathbf{v}_{ij} \cdot \mathbf{n}), \tag{2.21}$$

where $\mathbf{v}_{ij}$ is the relative contact force of the two interacting dilating spheres i and j, k_t is the tangential contact stiffness and $\mathbf{n}$ is the normal vector. In this case, k_t takes the form

$$k_t = \frac{2\left(G^2(1-\nu)|F_n|r_{ds}\right)^{1/3}}{2-\nu} \tag{2.22}$$

and the relative contact force $\mathbf{v}_{ij}$ is given as

$$\mathbf{v}_{ij} = \mathbf{v}_i - \mathbf{v}_j + r_i \times \boldsymbol{\omega}_i - r_j \times \boldsymbol{\omega}_j, \tag{2.23}$$

with $\mathbf{v}_i, \boldsymbol{\omega}_i$ and r_i the velocity, angular velocity and the distance between center and contact point of sphere i. Finally, the tangential contact force can then be expressed as

$$F_t^n = \min\left(|F_t^n|, |\mu F_n^n|\right) \cdot \mathbf{t}, \tag{2.24}$$

where $\mathbf{t}$ is the unit vector in tangential direction.

2.1.3 Angle of repose

The simulation model needs to be calibrated to the simulation case, including e.g. the particle material properties. One example of a parameter that affects the resulting contact force is the friction coefficient μ as introduced in Equation 2.18. A quantity that is commonly measured to calibrate the friction coefficient is the so-called *angle of repose*. It describes the steepest slope angle of a material heap on a horizontal plane without the heap collapsing. In other words, the angle of repose describes the maximum angle at which an object can be positioned on a tilting plane without sliding down.

As stated by Al-Hashemi and Al-Amoudi [48], the relation between friction coefficient μ and angle of repose θ is given as:

$$\tan(\theta) = \mu \tag{2.25}$$

In section 5.3 the angle of repose is an important calibration quantity to approximate the experimental results of a steel sheet under material flow.

2.1.4 Mass flow rate

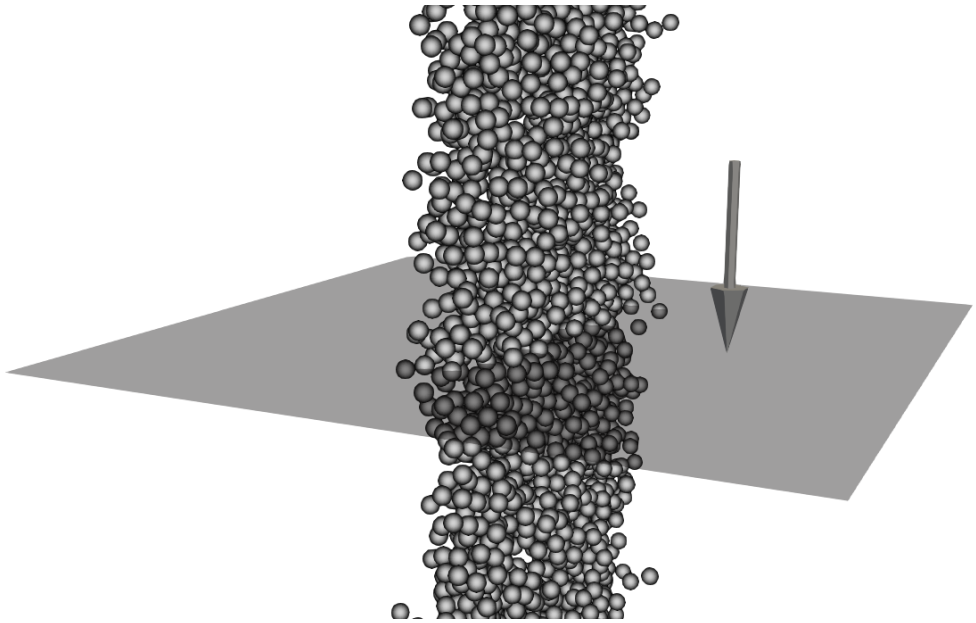

Figure 2.4: Illustration of the measurement of the mass flow rate. The mass flow rate of the spherical particles through the highlighted area is measured. The particles move from above the area downwards.

A second example of a calibration quantity for DEM is the *mass flow rate*. It measures the amount of mass passing a specified $2D$ area per time unit. An illustration of the mass flow rate measurement is given in Figure 2.4. The mass flow rate Φ is computed as

$$\Phi = \frac{\Delta m}{\Delta t}, \tag{2.26}$$

where Δt is a time interval and Δm the mass of particles passing the area in that time interval.

2.1.5 Rayleigh timestep

As we discussed before, the equations for explicit DEM are based on the assumption of a small enough simulation timestep. Thus, the DEM simulation is only stable for a timestep lower than a critical upper bound timestep. One concept of computing an upper bound for the critical timestep is the Rayleigh timestep as presented by Marigo and Stitt [49]. The Rayleigh timestep Δt_R is computed as

$$\Delta t_R = \frac{\pi R}{0.1631\nu + 0.8766}\sqrt{\frac{\rho_p}{G}}, \tag{2.27}$$

where R is the particle radius, ν the Poisson's ratio of the particle material, G the Shear modulus of the particle material and ρ_p the particle density.

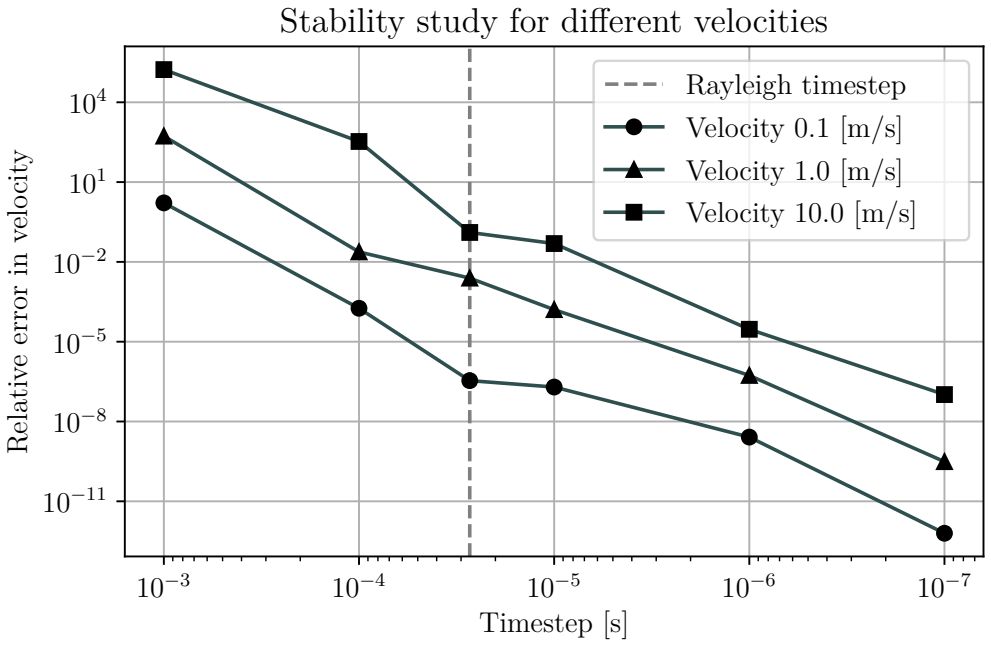

Figure 2.5: Convergence study of Demify® for different velocities for simulation of a single bouncing sphere. The Rayleigh timestep is included as vertical line.

In the computation of the Rayleigh timestep, no velocities are considered and it thus gives a good approximation for static particle simulations. However, for very dynamic cases with high velocities, the critical timestep is usually much lower than the Rayleigh timestep.

This is exemplified in Figure 2.5 where a convergence study concerning the timestep and the corresponding relative error for the DEM method implementation in Demify® was performed for different velocities. In this example, a sphere with a radius of 0.01 m, Poisson's ratio of 0.25, Young's modulus of 1 GPa and density of 1,000 kg/m^3

bounces back from a wall and the velocity after the bounce is evaluated. For a low velocity (0.1 m/s) of the sphere the relative error in the simulation of a bouncing sphere for the Rayleigh timestep is sufficiently low with a magnitude of approximately 10^{-6}. In contrast to that, for velocities with a higher magnitude (1 and 10 m/s), the relative error is quite large for the Rayleigh timestep and achieves a similar error as for 0.1 m/s with a timestep size of 10^{-6} or 10^{-7}, respectively. However, the Rayleigh timestep gives a first indication on a proper choice of a timestep as a function of material properties and needs to be adjusted to the expected particle velocities.

2.2 Finite Element Method for elastic problems

The finite element method is applied to solve partial differential equations (PDEs) describing continuous physical phenomena on given domains that represent the object of interest. The history of FEM starts back in 1956 when it was published in the well-known paper of Turner et al. [50] and the interest in the method was high. Especially for engineers FEM offered a possibility to handle the complex shapes of real designs [51]. Nowadays, usually deformations of materials and components due to loads or other acting forces are routinely analyzed with FEM.

Within this thesis, we only consider elastic problems and thus give a small overview of the most important terms for the theory of FEM for elastic problems in subsection 2.2.1. Elastic problems can be classified either as static or dynamic problems. Dynamic problems are solved with respect to a time increment and static problems are solved for a steady-state solution of the problem. The applications of this thesis are mainly dynamic problems which we also refer to as *transient*. In subsection 2.2.2 and subsection 2.2.3, we are concerned with deriving an expression for the stiffness matrix for both the static and the dynamic problem.

We give a short introduction into the theory of FEM following Ottosen and Petterson [52]. For simplicity we derive the systems of equations only for the linear elasticity theory, although non-linear models are applied within this thesis.

A common system of equations for a static case is

$$\mathbf{K}\mathbf{u} = \mathbf{F}, \tag{2.28}$$

where $\mathbf{K}$ is the *global stiffness matrix*, $\mathbf{u}$ is the displacement vector to be determined and $\mathbf{F}$ are the external forces acting on our object mesh.

For dynamic problems, the acceleration of an object must be taken into consideration, as this determines the velocity and position over time. Thus, a common system of equations for a dynamic case is

$$\mathbf{M}\ddot{\mathbf{u}}(t) + \mathbf{K}\mathbf{u}(t) = \mathbf{F}(t), \tag{2.29}$$

where $\mathbf{M}$ is the *global mass matrix*. A general FEM algorithm is summarized in Algorithm 2.

Algorithm 2 Pseudo-algorithm of a common FEM procedure.

1: Gather stiffness matrix by establishing stiffness relations for each element which depends on material properties and equilibrium conditions.
2: Assemble the system of equations:
3: Enforce compatibility as for instance a connected mesh.
4: Enforce equilibrium conditions at the nodal points.
5: Enforce boundary conditions on the system of equations.
6: Solve the system of equations.

2.2.1 Introduction to elasticity

Elastic problems are based on two physical quantities, *stress* and *strain*. While stress is a measure of the internal forces that act within the continuous material itself, strain describes a measure for the deformation of the material. Their mathematical formulation is given in the following.

The *strain* $\boldsymbol{\varepsilon}$ in $\mathbb{R}^3$ is a tensor of rank two with components

$$\boldsymbol{\varepsilon} = \begin{pmatrix} \varepsilon_{xx} & \varepsilon_{xy} & \varepsilon_{xz} \\ \varepsilon_{yx} & \varepsilon_{yy} & \varepsilon_{yz} \\ \varepsilon_{zx} & \varepsilon_{zy} & \varepsilon_{zz} \end{pmatrix}. \tag{2.30}$$

The *stress* $\boldsymbol{\sigma}$ in $\mathbb{R}^3$ is a tensor of rank two with components

$$\boldsymbol{\sigma} = \begin{pmatrix} \sigma_{xx} & \sigma_{xy} & \sigma_{xz} \\ \sigma_{yx} & \sigma_{yy} & \sigma_{yz} \\ \sigma_{zx} & \sigma_{zy} & \sigma_{zz} \end{pmatrix}, \tag{2.31}$$

where the components $\sigma_{xx}, \sigma_{yy}, \sigma_{zz}$ denote the *normal stresses* and the remaining ones the *shear stresses* [52].

As stated in Hughes [53], the strain tensor can be expressed in terms of the displacement vector: For higher dimension, let u_i denote the displacement in dimension i. Then the *infinitesimal strain tensor* $\boldsymbol{\varepsilon}_{ij}$ is defined as

$$\boldsymbol{\varepsilon}_{ij} \coloneqq \boldsymbol{\varepsilon}_{ij}(\mathbf{u}) = \frac{\partial_j u_i + \partial_i u_j}{2}, \tag{2.32}$$

for $i, j \in \{1, \ldots, n_d\}$ for n_d the space dimension, in our case $n_d = 3$. As indicated, we refer to the strain tensor from here on only as $\boldsymbol{\varepsilon}$ such that the dependence on the displacement $\mathbf{u}$ is implicit.

The stress describes the internal forces within an object due to external forces which then can cause deformations, i.e. strain. The stress-strain relation can be described by the *generalized Hooke's law* [52] as

$$\boldsymbol{\sigma}_{ij} = \sum_{k,l=1}^{n_d} \mathbf{C}_{ijkl} \boldsymbol{\varepsilon}_{kl}, \tag{2.33}$$

where $\mathbf{C}$ denotes the fourth-order tensor of elastic moduli and $i, j, k, l \in \{1, \ldots, n_d\}$. For better readability, we omit the sum over k, l in later equations and indicate it by the indices k, l themselves. The strain energy function in multiple dimensions then takes the form

$$w_{ij} = \int \mathbf{C}_{ijkl}\boldsymbol{\varepsilon}_{kl}\,\mathrm{d}\,\boldsymbol{\varepsilon}_{ij} = \frac{1}{2}\mathbf{C}_{ijkl}\boldsymbol{\varepsilon}_{ij}\boldsymbol{\varepsilon}_{kl} \tag{2.34}$$

and is non-negative provided $\mathbf{C}$ is positive-definite.

For *isotropic* object materials, meaning that the material has no preferred orientations or directions, $\mathbf{C}$ is computed as

$$\mathbf{C}_{ijkl} = \lambda\delta_{ij}\delta_{kl} + \mu\left(\delta_{ik}\delta_{jl} + \delta_{il}\delta_{jk}\right), \tag{2.35}$$

with λ, μ the two independent *Lamé constants* and δ the Kronecker delta. The Lamé constants are computed as follows:

$$\mu = \frac{E}{2(1+\nu)}, \qquad \lambda = \frac{\nu E}{(1+\nu)(1-2\nu)}, \tag{2.36}$$

for ν the material's Poisson's ratio and E its Young's modulus. Finally, the stress-strain relation for an isotropic elastic material is then given as

$$\boldsymbol{\sigma}_{ij} = \mathbf{C}_{ijkl}\boldsymbol{\varepsilon}_{kl} = \lambda\boldsymbol{\varepsilon}_{kk}\delta_{ij} + 2\mu\boldsymbol{\varepsilon}_{ij}. \tag{2.37}$$

2.2.2 Elastostatics

Based on Equation 2.37, we can formulate a partial differential equation for an elastic body in static equilibrium. Given a PDE system, we follow Hughes [53] to deduce the final system of equations to solve as stated in Equation 2.28.

The equation system for elastostatics reads

$$\partial_j\boldsymbol{\sigma}_{ij} + f_i = 0 \text{ in } \Omega \qquad \text{for } i, j = 1, \ldots, n_d, \tag{2.38}$$

$$u_i = g_i \text{ on } \Gamma_{g_i} \qquad \text{for } i = 1, \ldots, n_d, \tag{2.39}$$

$$\boldsymbol{\sigma}_{ij}\mathbf{n}_j = h_i \text{ on } \Gamma_{h_i}, \qquad \text{for } i, j = 1, \ldots, n_d, \tag{2.40}$$

where $\mathbf{n}_j$ is the jth component of the normal vector, $g_i : \Gamma_{g_i} \to \mathbb{R}, h_i : \Gamma_{h_i} \to \mathbb{R}$ are the *prescribed boundary displacements* and

$$\Gamma = \overline{\Gamma_{g_i} \cup \Gamma_{h_i}} \qquad \forall i = 1, \ldots, n_d \tag{2.41}$$

is the boundary of the domain $\Omega \subset \mathbb{R}^{n_d}$ and $u : \Omega \to \mathbb{R}$.

In our applications, we can interpret g_i as clamp boundary conditions and h_i as the incoming point forces or pressures as boundary condition. The force vector f_i describes forces acting on the whole object and not only the boundary, most commonly gravity.

Let us now formulate the weak form for the elastostatic problem given the strong form in Equation 2.38 - Equation 2.40. To do so, we denote the solution space for

dimension i as $\mathbb{S}_i$ and the variation space for dimension i as $\mathbb{V}_i$. All $u_i \in \mathbb{S}_i$ satisfy boundary condition 2.39 and all $v_i \in \mathbb{V}_i$ satisfy $v_i = 0$ on Γ_{g_i}. Then, the weak formulation is

$$\sum_{i,j=1}^{n_d} \int_\Omega \frac{\partial_j v_i + \partial_i v_j}{2} \boldsymbol{\sigma}_{ij} \,\mathrm{d}\,\Omega = \sum_{i=1}^{n_d} \int_\Omega v_i f_i \,\mathrm{d}\,\Omega + \sum_{i=1}^{n_d} \int_{\Gamma_{h_i}} v_i h_i \,\mathrm{d}\,\Gamma. \tag{2.42}$$

Let $\mathbb{S} = \{\mathbf{u} \mid \mathbf{u}_i \in \mathbb{S}_i\}$ and $\mathbb{V} = \{\mathbf{v} \mid \mathbf{v}_i \in \mathbb{V}_i\}$. Then, we can express the weak form from Equation 2.42 with the symmetric bilinear form a and linear forms as

$$a(\mathbf{v}, \mathbf{u}) = (\mathbf{v}, \mathbf{f}) + (\mathbf{v}, \mathbf{h})_\Gamma \tag{2.43}$$

where the bilinear form is defined as:

$$a(\mathbf{v}, \mathbf{u}) \coloneqq \sum_{i,j=1}^{n_d} \int_\Omega \frac{\partial_j v_i + \partial_i v_j}{2} \boldsymbol{\sigma}_{ij} \,\mathrm{d}\,\Omega, \tag{2.44}$$

and the linear forms as:

$$(\mathbf{v}, \mathbf{f}) \coloneqq \sum_{i=1}^{n_d} \int_\Omega v_i f_i \,\mathrm{d}\,\Omega, \tag{2.45}$$

$$(\mathbf{v}, \mathbf{h})_\Gamma \coloneqq \sum_{i=1}^{n_d} \int_{\Gamma_{h_i}} v_i h_i \,\mathrm{d}\,\Gamma. \tag{2.46}$$

Note that the stress tensor $\boldsymbol{\sigma}$ is dependent on the displacement u, since the stress tensor is defined through the strain tensor $\boldsymbol{\varepsilon}$. In Equation 2.32 we introduced the definition of the strain tensor based on the displacement. Thus, for clarity, Equation 2.44 can also be expressed as

$$a(\mathbf{v}, \mathbf{u}) = \sum_{i,j=1}^{n_d} \int_\Omega \frac{\partial_j v_i + \partial_i v_j}{2} \mathbf{C}_{ijkl} \frac{\partial_j u_i + \partial_i u_j}{2} \,\mathrm{d}\,\Omega. \tag{2.47}$$

Let now $\mathbb{S}^h$ and $\mathbb{V}^h$ be finite-dimensional approximations of $\mathbb{S}$ and $\mathbb{V}$. Elements $\mathbf{v}^h \in \mathbb{V}^h$ fulfill $\mathbf{v}_i^h = 0$ on Γ_{g_i} and for elements of $\mathbb{S}^h$ the composition

$$\mathbf{u}^h = \mathbf{w}^h + \mathbf{g}^h \tag{2.48}$$

holds for $\mathbf{w}^h \in \mathbb{V}^h$ and $\mathbf{g}^h$ an approximation of the boundary condition, Equation 2.39. Utilizing the composition from above, we can express the *Galerkin formulation* of the problem as: Given $\mathbf{f}, \mathbf{g}$ and $\mathbf{h}$, find $\mathbf{u}^h = \mathbf{w}^h + \mathbf{g}^h, \mathbf{u}^h \in \mathbb{S}^h$ such that for all $\mathbf{v}^h \in \mathbb{V}^h$ it holds

$$a(\mathbf{v}^h, \mathbf{w}^h) = (\mathbf{v}^h, \mathbf{f}) + (\mathbf{v}^h, \mathbf{h})_\Gamma - a(\mathbf{v}^h, \mathbf{g}^h). \tag{2.49}$$

Now that we have the Galerkin formulation of the elastostatic problem, we can rearrange it to define the stiffness matrix $\mathbf{K}$. Let us denote the standard basis

vectors of $\mathbb{R}^{n_d}$ as $\{\mathbf{e}_i\}_{i=1}^{n_d}$. Then, the functions $\mathbf{v}^h \in \mathbb{S}^h$ and $\mathbf{w}^h \in \mathbb{V}^h$ can be expressed as

$$\mathbf{v}^h = \sum_{i=1}^{n_d} v_i^h \mathbf{e}_i, \tag{2.50}$$

$$\mathbf{w}^h = \sum_{i=1}^{n_d} w_i^h \mathbf{e}_i. \tag{2.51}$$

Let us denote the basis of the variation space as $\{N_A\}_{A=1}^{n_n} \subset \mathbb{V}^h$ for n_n the number of nodes in the object mesh. The basis functions N_A are also referred to as *shape functions*. Every variation function $w^h \in \mathbb{V}^h$ can then be expressed uniquely in terms of the basis of shape functions. To utilize the composition (see Equation 2.48) of the displacement vector, let us divide the set of mesh nodes η (of size n_n) into two complementing subsets. Let $\eta_{g_i} \subset \eta$ be the set of nodes for which the displacement vector fulfills the boundary condition from Equation 2.39. Thus, for the nodes in η_{g_i} it holds $u_i^h = g_i$. Then, $\eta_{g_i}^c := \eta - \eta_{g_i}$ denotes the complement of η_{g_i} and let us denote its size by $n_c \leq n_n$. Thus, each u_i^h for $i = 1, \ldots, n_d$ must be determined for all nodes A in $\eta_{g_i}^c$. Let us denote the nodal values of w_i^h and g_i^h as d_{iA} and g_{iA} respectively for i the space dimension index and A the node index. Then, we can express w_i^h and g_i^h in terms of nodal shape functions as

$$w_i^h = \sum_{A \in \eta_{g_i}^c} N_A d_{iA}, \tag{2.52}$$

$$g_i^h = \sum_{A \in \eta_{g_i}} N_A g_{iA} \tag{2.53}$$

for $i = 1, \ldots, n_d$. With the new expressions of the functions, we can rewrite the Galerkin Equation 2.49 as follows:

$$\begin{aligned} &\sum_{j=1}^{n_d} \sum_{B \in \eta_{g_i}^c} a\left(N_A \mathbf{e}_i, N_B \mathbf{e}_j\right) d_{jB} \\ &\qquad = \left(N_A \mathbf{e}_i, \mathbf{f}\right) + \left(N_A \mathbf{e}_i, \mathbf{h}\right)_\Gamma - \sum_{j=1}^{n_d} \sum_{B \in \eta_{g_i}} a\left(N_A \mathbf{e}_i, N_B \mathbf{e}_j\right) g_{jB}, \end{aligned} \tag{2.54}$$

for all $A \in \eta_{g_i}^c$ and $i = 1, \ldots, n_d$.

Let us denote the global node indices as $P, Q = 1, \ldots, n_d \cdot n_c$. Each global node index P corresponds to a mesh node $A \in \eta_{g_i}^c$ and a dimension $i \in \{1, \ldots, n_d\}$. Similarly, we have the convention that the global index Q corresponds to node B and dimension j. The system of equations as in Equation 2.28 is then given as

$$\mathbf{K}\mathbf{u} = \mathbf{F}, \tag{2.55}$$

with $\mathbf{K} \in \mathbb{R}^{n_d \cdot n_c \times n_d \cdot n_c}, \mathbf{u} \in \mathbb{R}^{n_d \cdot n_c}, \mathbf{F} \in \mathbb{R}^{n_d \cdot n_c}$. The entries of $\mathbf{K}$ and $\mathbf{F}$ take the form:

$$\mathbf{K}_{PQ} = a\left(N_A \mathbf{e}_i, N_B \mathbf{e}_j\right), \tag{2.56}$$

$$\mathbf{F}_P = \left(N_A \mathbf{e}_i, \mathbf{f}\right) + \left(N_A \mathbf{e}_i, \mathbf{h}\right)_\Gamma - \sum_{j=1}^{n_d} \sum_{B \in \eta_{g_i}} a\left(N_A \mathbf{e}_i, N_B \mathbf{e}_j\right) g_{jB}. \tag{2.57}$$

2.2.3 Elastodynamics

In the previous section we considered the equations for an elastic body in static equilibrium. In this section, we deduce the equation system for an elastic body with variation in time. The main difference between the equation systems of elastostatics and elastodynamics is the addition of the mass matrix term [53]. When investigating dynamic simulation cases, one needs to consider besides the displacement $u_i : \Omega \times (0,T) \to \mathbb{R}$ also the velocities and accelerations $\dot{u}_i, \ddot{u}_i : \Omega \times (0,T) \to \mathbb{R}$, with $i = 1, \ldots, n_d$. The initial displacement and velocity are given by the superscript 0 as $u_i^0 : \Omega \to \mathbb{R}$ and $\dot{u}_i^0 : \Omega \to \mathbb{R}$. The remaining data that we had before, now takes the form

$$f_i : \Omega \times (0,T) \to \mathbb{R}, \tag{2.58}$$
$$g_i : \Gamma_{g_i} \times (0,T) \to \mathbb{R}, \tag{2.59}$$
$$h_i : \Gamma_{h_i} \times (0,T) \to \mathbb{R}. \tag{2.60}$$

Additionally to the previous case, we now also consider the density of the object's material $\rho_s : \Omega \to \mathbb{R}_{>0}$.

Then, the initial boundary value problem is given as

$$\rho_s \ddot{u}_i = \partial_j \boldsymbol{\sigma}_{ij} + f_i \qquad \text{on } \Omega \times (0,T) \tag{2.61}$$
$$u_i = g_i \qquad \text{on } \Gamma_{g_i} \times (0,T) \tag{2.62}$$
$$\boldsymbol{\sigma}_{ij} \mathbf{n}_j = h_i \qquad \text{on } \Gamma_{h_i} \times (0,T) \tag{2.63}$$
$$u_i(\mathbf{x}, 0) = u_i^0(\mathbf{x}) \qquad \text{for } \mathbf{x} \in \Omega \tag{2.64}$$
$$\dot{u}_i(\mathbf{x}, 0) = \dot{u}_i^0(\mathbf{x}) \qquad \text{for } \mathbf{x} \in \Omega. \tag{2.65}$$

where the stress tensor $\boldsymbol{\sigma}$ is as before and $i, j = 1, \ldots, n_d$. Equation 2.61 is the *equation of motion*.

As before, we define the solution and variation space, in this case though with consideration of the time $t \in (0,T)$. Let $\mathbb{S}_t$ be the solution space at time t and $\mathbb{V}$ the variation space. Given the boundary and initial conditions $\mathbf{f}, \mathbf{g}, \mathbf{h}, \mathbf{u}^0$ and $\dot{\mathbf{u}}^0$, we want to find the solution of the displacement $\mathbf{u}(t) \in \mathbb{S}_t$ such that for all test functions $\mathbf{v} \in \mathbb{V}$ the weak formulation

$$(\mathbf{v}, \rho_s \ddot{\mathbf{u}}) + a(\mathbf{v}, \mathbf{u}) = (\mathbf{v}, \mathbf{f}) + (\mathbf{v}, \mathbf{h})_\Gamma \tag{2.66}$$

with initial conditions

$$(\mathbf{v}, \rho_s \mathbf{u}(0)) = (\mathbf{v}, \rho_s \mathbf{u}^0) \tag{2.67}$$
$$(\mathbf{v}, \rho_s \dot{\mathbf{u}}(0)) = (\mathbf{v}, \rho_s \dot{\mathbf{u}}^0) \tag{2.68}$$

is satisfied. The bilinear form and linear forms are defined as before, see Equation 2.44 - Equation 2.46.

Analogously to the static case, let us define the finite-dimensional space approximations $\mathbb{S}_t^h$ of $\mathbb{S}_t$ and $\mathbb{V}^h$ of $\mathbb{V}$. For elements $\mathbf{u}^h(t) \in \mathbb{S}_t^h$ the composition

$$\mathbf{u}^h = \mathbf{w}^h + \mathbf{g}^h \tag{2.69}$$

holds for $\mathbf{w}^h \in \mathbb{V}^h$ and $\mathbf{g}^h$ an approximation of the boundary condition of Equation 2.62.

Given the composition of Equation 2.69 and the sum rule of derivatives, we get the following *semi-discrete* Galerkin formulation: Given $\mathbf{f}, \mathbf{g}, \mathbf{h}, \mathbf{u}^0$ and $\dot{\mathbf{u}}^0$, find $\mathbf{u}^h = \mathbf{w}^h + \mathbf{g}^h, \mathbf{u}^h \in \mathbb{S}_t^h$ such that for all $\mathbf{v}^h \in \mathbb{V}^h$ it holds

$$(\mathbf{v}^h, \rho_s \ddot{\mathbf{w}}^h) + a(\mathbf{v}^h, \mathbf{w}^h) = (\mathbf{v}^h, \mathbf{f}) + (\mathbf{v}^h, \mathbf{h})_\Gamma - (\mathbf{v}^h, \rho_s \ddot{\mathbf{g}}^h) - a(\mathbf{v}^h, \mathbf{g}^h) \tag{2.70}$$

with

$$(\mathbf{v}^h, \rho_s \mathbf{w}^h(0)) = (\mathbf{v}^h, \rho_s \mathbf{u}^0) - (\mathbf{v}^h, \rho_s \mathbf{g}^h(0)), \tag{2.71}$$

$$(\mathbf{v}^h, \rho_s \dot{\mathbf{w}}^h(0)) = (\mathbf{v}^h, \rho_s \dot{\mathbf{u}}^0) - (\mathbf{v}^h, \rho_s \dot{\mathbf{g}}^h(0)). \tag{2.72}$$

The formulation is semi-discrete as we only discretized the problem in space and not yet in time. The time discretization is done by time integration. The time step method used within this thesis for structural dynamics is a variant of the Newmark method [54] which is implicit.

Following the arguments of the formulation of Equation 2.52 and Equation 2.53, we can express $\mathbf{v}^h$ and $\mathbf{g}^h$ as

$$v_i^h(\mathbf{x}, t) = \sum_{A \in \eta_{g_i}^c} N_A(\mathbf{x}) d_{iA}(t), \tag{2.73}$$

$$g_i^h(\mathbf{x}, t) = \sum_{A \in \eta_{g_i}} N_A(\mathbf{x}) g_{iA}(t), \tag{2.74}$$

with $d_{iA}(t)$ the nodal value of v_i^h and $g_{iA}(t)$ the nodal value of g_i^h at time t. Then, the equation system in matrix form reads

$$\mathbf{M}\ddot{\mathbf{d}}(t) + \mathbf{K}\mathbf{d}(t) = \mathbf{F}(t) \tag{2.75}$$

$$\mathbf{d}(0) = \mathbf{d}^0 \tag{2.76}$$

$$\dot{\mathbf{d}}(0) = \dot{\mathbf{d}}^0. \tag{2.77}$$

$\mathbf{M}$ is referred to as *mass matrix*.

The entries of $\mathbf{K}$ are as in Equation 2.56. The entries of $\mathbf{M}$ and $\mathbf{F}$ take the following form:

$$\mathbf{M}_{PQ} = (N_A \mathbf{e}_i, \rho_s N_B \mathbf{e}_j) \tag{2.78}$$

$$\mathbf{F}_P = (N_A \mathbf{e}_i, \mathbf{f}) + (N_A \mathbf{e}_i, \mathbf{h})_\Gamma - \sum_Q (\mathbf{K}_{PQ} g_Q + \mathbf{M}_{PQ} \ddot{g}_Q) \tag{2.79}$$

$\mathbf{d}^0$ and $\dot{\mathbf{d}}^0$ are given by

$$\mathbf{d}^0 = \mathbf{M}^{-1}\mathbf{D}^0, \qquad \dot{\mathbf{d}}^0 = \mathbf{M}^{-1}\dot{\mathbf{D}}^0, \tag{2.80}$$

with

$$\mathbf{D}_P^0 = (N_A \mathbf{e}_i, \rho_s u_i^0) - \sum_Q \mathbf{M}_{PQ} g_Q(0), \tag{2.81}$$

$$\dot{\mathbf{D}}_P^0 = (N_A \mathbf{e}_i, \rho_s \dot{u}_i^0) - \sum_Q \mathbf{M}_{PQ} \dot{g}_Q(0). \tag{2.82}$$

2.2.4 Shell elements

The system of equations we deduced for elasticity in the previous chapters, are for volume mesh elements when $n_d = 3$. Another type of 3D mesh elements are *shell elements* which are faces, usually quadrilaterals or triangles. Given the shell elements and a mesh thickness, the mesh can be extended to a volume with the given thickness. An illustration of the volume resulting from a shell mesh is given in Figure 2.6 where the original shell mesh is represented by the mid-surface mesh with white filled nodes. The two newly created surfaces are referred to as *reference surface* [51] and visualized as the smaller black nodes in Figure 2.6.

(a) Original mesh **(b)** Deformed mesh

Figure 2.6: Illustration of a shell element mesh with the original shell nodes as mid-surface nodes (white filled nodes) and upper and lower reference surface nodes (black nodes).

The system of equations is only solved for the mid-surface, which is the actual shell element mesh. To deduce the positions of the reference surfaces after a deformation as in Figure 2.6, the rotation of the original nodes are required as well as the position. Together with the thickness, the new position of the node is uniquely determined.

2.2.5 Numerical damping

Damping methods can be introduced to prevent an algorithm from getting unstable. Instabilities can occur for instance due to high frequencies or extreme forces. As deduced in the previous sections, the system of equations for a dynamic case is given as Equation 2.29. When damping is introduced, the system can take the following form instead:

$$\mathbf{M}\ddot{\mathbf{u}}(t) + \mathbf{C}\dot{\mathbf{u}}(t) + \mathbf{K}\mathbf{u}(t) = \mathbf{F}(t), \tag{2.83}$$

for a *damping matrix* $\mathbf{C}$.

A common damping method is the *Rayleigh damping* that defines the damping matrix $\mathbf{C}$ as

$$\mathbf{C} \coloneqq \vartheta\mathbf{M} + \xi\mathbf{K}, \tag{2.84}$$

where ϑ, ξ are constants of proportionality.

The time stepping scheme with numerical damping applied within this thesis is the extension of Newmark's method as suggested by Bossak, see Wood, Bossak, and

Zienkiewicz [54]. We denote the three timestep parameters by α, β, γ. The *Bossak-Newmark damping* algorithm then takes the form

$$\mathbf{u}_{n+1} = \mathbf{u}_n + \Delta t \mathbf{u}_n + (\Delta t)^2 \left(\frac{1}{2} - \beta\right) \ddot{\mathbf{u}}_n + (\Delta t)^2 \beta \ddot{\mathbf{u}}_{n+1}, \tag{2.85}$$

$$\dot{\mathbf{u}}_{n+1} = \dot{\mathbf{u}}_n + \Delta t(1-\gamma)\ddot{\mathbf{u}}_n + \Delta t \gamma \ddot{\mathbf{u}}_{n+1} \tag{2.86}$$

and the system of equations to solve for is

$$(1-\alpha)\mathbf{M}\ddot{\mathbf{u}}_{n+1} + \alpha \mathbf{M}\ddot{\mathbf{u}}_n + \mathbf{C}\dot{\mathbf{u}}_{n+1} + \mathbf{K}\mathbf{u}_n = \mathbf{F}_{n+1}, \tag{2.87}$$

where the indices indicate the timestep, e.g. $\mathbf{u}_n = \mathbf{u}(t_n)$. We choose the parameters β, γ in dependence of α as

$$\gamma = 0.5 - \alpha \qquad \text{and } \beta = 0.5\gamma + 0.01. \tag{2.88}$$

The method with this parameter choice is unconditionally stable [54].

3

DEM-FEM Coupling

The DEM-FEM coupling scheme combines DEM and FEM and enables communication between the two solvers. DEM simulates granular media and the forces resulting from contacts between particles and the object of the FEM domain are collected and transferred to FEM. FEM then simulates the object with the forces as boundary conditions and the movement of the object is returned to DEM. The exact order and variations of this scheme are discussed in section 3.1. After introducing the general coupling scheme, we formulate the coupling algorithm for the scheme more specifically in section 3.2. Then in section 3.3, we give some insights into implementation details that are specific for the DEM and FEM software that we apply. In section 3.4 we discuss the advantages and drawbacks of our coupling formulation and finally conclude with a general workflow description for new simulation cases in section 3.5.

3.1 Time scheme overview

To give a first overview of the coupling algorithm, we illustrate the different steps along a timeline in Figure 3.1. In Figure 3.1a the *just-in-time coupling* scheme is illustrated which is in general the first coupling approach within this thesis. The *predictive coupling* illustrated in Figure 3.1b is a similar coupling approach with an adaptation of the movement data handed over to DEM. That the data is not handed over as obtained from FEM, but altered is marked with *.

The general setup for both coupling schemes is the same. There are three timelines in total, the first timeline t for the general simulation time, a timeline t^D for the DEM solver time and timeline t^F for the FEM solver. In total, the initial timestep t_0 and three full timesteps are visualized, t_1, t_2 and t_3. At the initialization, we transfer the FEM object's triangle mesh to the DEM solver which is indicated with the green arrow "Init object".

In the just-in-time coupling each iteration consists of four steps. First, n^D timesteps are simulated in DEM. Then, the forces arising from contacts between object and particles are accumulated and provided to the FEM solver. With the FEM solver we simulate one timestep and hand over the object node's positions, velocities and accelerations to the DEM solver.

Similarly, each iteration of the predictive coupling consists of four steps. First of all, one timestep is simulated with the FEM solver. The initial position of the object in

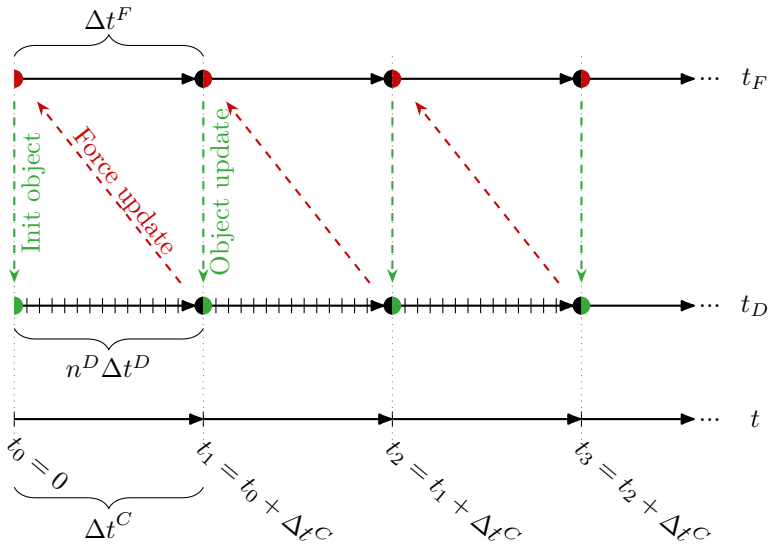

(a) Illustration of the just-in-time coupling scheme.

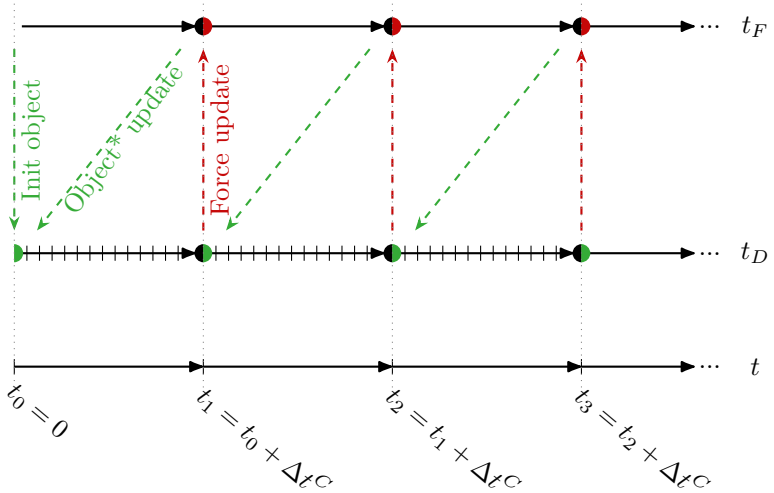

(b) Illustration of the predictive coupling scheme. The * indicates that the object movement data is altered before given to DEM.

Figure 3.1: Illustration of coupling schemes, inspired by [26].

this iteration and the resulting one are combined to calculate a predictive velocity. It describes the velocity of the object that is required at the start of this iteration to arrive at its resulting position. Then, the position and velocity are provided to the object in the DEM solver. With the DEM solver we simulate n^D timesteps and accumulate the contact forces acting onto the FEM object and hand them over to the FEM solver.

Another variant of both the just-in-time coupling and predictive coupling is *force averaging*. In more detail, the mean of the forces that act on the object over all n^D DEM timesteps is computed and given as boundary condition to FEM instead of only the force of the last DEM timestep.

3.2 Detailed algorithm

In the last section we got an overview on how the coupling is executed, illustrated over a timeline. To give a more detailed understanding, we introduce a pseudo-algorithm in this section, with which we elaborate the individual steps.

We consider the just-in-time coupling first and then later on make some notes on changes that occur when using the predictive coupling or force averaging instead.

Algorithm 3 Just-in-time coupling algorithm

Require: $\Delta t^C, \Delta t^F, \Delta t^D, t_T, M^F$

Let $n_D \coloneqq \Delta t^C / \Delta t^D$

$T^D \leftarrow T^F\left(M^F\right)$

Let $t_i, t_{i+1} \coloneqq 0$

while $t_i < t_T$ **do**

  Simulate n^D steps in DEM timestep Δt^D

  Transfer forces from DEM to FEM triangle mesh:

$$(\mathbf{F}_{T^F})_i \leftarrow (\mathbf{F}_{T^D})_{i+1}$$

  Simulate one step in FEM with a timestep of Δt^F

  Transfer object movement from FEM to DEM:

$$\begin{aligned}(\mathbf{P}_{T^D})_{i+1} &\leftarrow (\mathbf{P}_{T^F})_{i+1}\\ (\mathbf{V}_{T^D})_{i+1} &\leftarrow (\mathbf{V}_{T^F})_{i+1}\\ (\mathbf{A}_{T^D})_{i+1} &\leftarrow (\mathbf{A}_{T^F})_{i+1}\end{aligned}$$

  $t_i \leftarrow t_i + \Delta t^C$

end while

First of all, we define the different time steps. We denote the DEM timestep by Δt^D and the FEM timestep by Δt^F, where the latter also defines the coupling timestep Δt^C. The FEM timestep must be a multiple of the DEM timestep. Thus, in total we have these two requirements on the timestep choice:

$$\Delta t^C \coloneqq \Delta t^F \tag{3.1}$$

Let $n^D > 0$ be a natural number. Δt^D is then required to fulfill

$$\Delta t^F = n^D \cdot \Delta t^D. \tag{3.2}$$

To start the coupling, the timesteps $\Delta t^C, \Delta t^F$ and Δt^D and total simulation time t_T must be given as denoted in the requirements of Algorithm 3. Furthermore, a mesh M^F for the FEM object is required. In line 1 of Algorithm 3 we deduce the number of DEM timesteps n^D that are performed between each coupling step. We initialize the DEM triangle mesh T^D in line 2 by extracting the exterior surface triangulation T^F of M^F.

At this point the actual coupled simulation starts and simulates until time t_T. The coupling and data exchange between the two solvers are performed after each coupling timestep Δt^C. In line 5 the DEM solver simulates n^D timesteps of size Δt^D from the current time t_i until the next time t_{i+1}. T^D is updated continuously and thus moving during the DEM simulation based on its initial position, velocity and acceleration.

We denote the force acting on the mesh T^D caused by contacts with particles at time t_i by $(\mathbf{F}_{T^D})_i$. After simulating DEM the forces $(\mathbf{F}_{T^D})_{i+1}$ on the mesh at time t_{i+1} are gathered and assigned in line 6 as boundary conditions onto the FEM object by

$$(\mathbf{F}_{T^F})_i \leftarrow (\mathbf{F}_{T^D})_{i+1} \tag{3.3}$$

In line 7, one step is simulated with the FEM solver with a timestep of size Δt^F. As the nodes' positions, velocities and accelerations have been updated within the FEM simulation, this information needs to be transferred to the DEM solver, which is performed in line 8. Since at this point the FEM solver has arrived at time t_{i+1}, the positions $(\mathbf{P}_{T^F})_{i+1}$, velocities $(\mathbf{V}_{T^F})_{i+1}$, accelerations $(\mathbf{A}_{T^F})_{i+1}$ of the FEM surface triangulation at that time are assigned to $(\mathbf{P}_{T^D})_{i+1}, (\mathbf{V}_{T^D})_{i+1}, (\mathbf{A}_{T^D})_{i+1}$ of the DEM triangle mesh at that time.

Finally, the current time can be updated as done in line 9 and the coupling and information exchange is completed for this iteration.

When considering the predictive coupling, the order of lines 5 - 8 changes to 7, 8, 5, 6. Thus, a coupling step starts with the execution of one FEM simulation step. Instead of transferring the position, velocity and acceleration of the object, a predictive velocity $\mathbf{V}_{0,1}$ is computed based on the initial position $\mathbf{P}_0$ and the resulting position $\mathbf{P}_1$ of the object in this iteration. The predictive velocity is defined as

$$\mathbf{V}_{0,1} \coloneqq \frac{\mathbf{P}_1 - \mathbf{P}_0}{\Delta t^F} \tag{3.4}$$

Then, line 8 takes instead the form

$$(\mathbf{P}_{T^D})_i \leftarrow (\mathbf{P}_{T^F})_i, \tag{3.5}$$

$$(\mathbf{V}_{T^D})_i \leftarrow \frac{(\mathbf{P}_{T^F})_{i+1} - (\mathbf{P}_{T^F})_i}{\Delta t^F}, \tag{3.6}$$

$$(\mathbf{A}_{T^D})_i \leftarrow \mathbf{0}. \tag{3.7}$$

This ensures that the object in DEM starts and ends at the exact same position as the FEM object reducing the risk of diverging objects within the two solvers.

In the case of force averaging, the forces over the n^D timesteps in line 5 need to be summed up in order to compute the mean. Then, line 6 is changed to

$$\mathbf{F}_{T^F}(t_i) \leftarrow \frac{1}{n^D} \sum_{j=1}^{n^D} \mathbf{F}_{T^D}(t_i + j\Delta t^D), \tag{3.8}$$

with $\mathbf{F}_{T^F}(t_i) \coloneqq (\mathbf{F}_{T^F})_i$.

3.3 Implementation details

In the previous section we described the general coupling algorithm developed in this thesis for general DEM and FEM solvers. Within this thesis we apply the FCC in-house solvers Demify® and LaStFEM. The coupling algorithm is specifically adapted to these solvers and some further explanation follows in this section on the details of some operations.

3.3.1 Triangle mesh

The first step in the coupling algorithm is to transfer the exterior surface triangulation from FEM to DEM. In DEM a flexible object is created based on the triangle mesh geometry. The term flexible object describes a solid object whose positions, velocities and accelerations for all nodes can be set individually during runtime.

Since several DEM timesteps are run before coupling to FEM, the positions between the two meshes will slightly drift apart for the just-in-time coupling. Although Demify® considers the velocity and acceleration to move the mesh during the DEM simulation, the integration model slightly differs from the one implemented in LaStFEM. This small difference will be corrected in the next coupling step when besides velocity and acceleration also the position gets updated.

However, if the drift in positions gets too large, the correction in the position update can cause an extreme overlap between the object and particles. This in turn can result in extreme forces acting on the mesh, leading to instabilities. To avoid large drifts in positions, numerical damping as explained in subsection 2.2.5 can be introduced to prevent large accelerations. Another method to avoid drifting positions is the usage of the predictive coupling, where no acceleration appears in the DEM simulation and the velocities are prescribed to move the object to the exact position of the FEM object.

3.3.2 Force transfer

As elaborated in subsection 2.1.2, contacts between particles and the flexible object result in forces. These forces are accumulated by Demify® for each node of the flexible object triangle mesh in each timestep. When coupling to FEM, the current forces are transferred such that they apply on the FEM object.

For volume element meshes, the forces can be transferred 1:1 as the exterior volume nodes coincide with the exterior surface triangulation nodes. Thus, the forces are applied as point force boundary conditions on the exterior nodes of M^F.

However, for shell element meshes the force transfer is slightly more complex. In subsection 2.2.4 we described the different structure of shell element meshes. Thus, the force transfer onto the mesh nodes is adapted to that structure for shell elements. Let $n_{s,i}, n_{m,i}, n_{r,i}$ be the original shell element, corresponding mid-surface and corresponding reference node. We refer to the nodes analogously as to the surfaces in subsection 2.2.4. The force on the mid-surface node $n_{m,i}$ is then assembled as the sum of the forces acting on the original shell element and reference node:

$$\mathbf{F}_{T^F|_{n_{m,i}}} = \mathbf{F}_{T^F|_{n_{s,i}}} + \mathbf{F}_{T^F|_{n_{r,i}}}. \tag{3.9}$$

3.4 Scheme discussion

The motivation why we choose the coupling algorithm as described in the previous section is that it does not require changes in the solver cores at hand. All functionalities needed are getters and setters of the object movement and forces that are existent in both solvers. Any other manipulation as performed in the predictive coupling or with force averaging does not affect the solvers.

However, there are also some drawbacks. We cannot parallelize the coupling algorithm as data transfers are done between the different solver calls.

An option to optimize the coupling algorithm is the implementation of a predictor-corrector method. This would include that for instance a prediction of the object's movement is computed by DEM, that is then corrected by the actual movement obtained from the FEM simulation. Then, the prediction and correction can be performed again, e.g. until convergence. This would increase the order of accuracy of the coupling algorithm, but would lead to longer computation times.

3.5 Workflow

The workflow applied in this thesis for each new simulation case for the DEM-FEM coupling is visualized in Figure 3.2. The process of setting up a simulation case, running it and analyzing the results consists of several steps. The steps that are performed within this thesis are highlighted as gray boxes. Steps that are performed externally, meaning that only the result is given and used further within this thesis, are highlighted as white boxes with a dashed border. The steps are structured in four parts, specifically pre-processing, simulation preparation, DEM-FEM coupling and post-processing.

During the pre-processing, we are concerned with gathering all geometries needed for the specific simulation case. That process starts with the creation of CAD geometries that describe the objects as for instance, a sleeper. After receiving the CAD geometries, the ones meant for the DEM simulation - domain boundaries and particle geometries - are converted to triangle meshes saved as STL files. The one

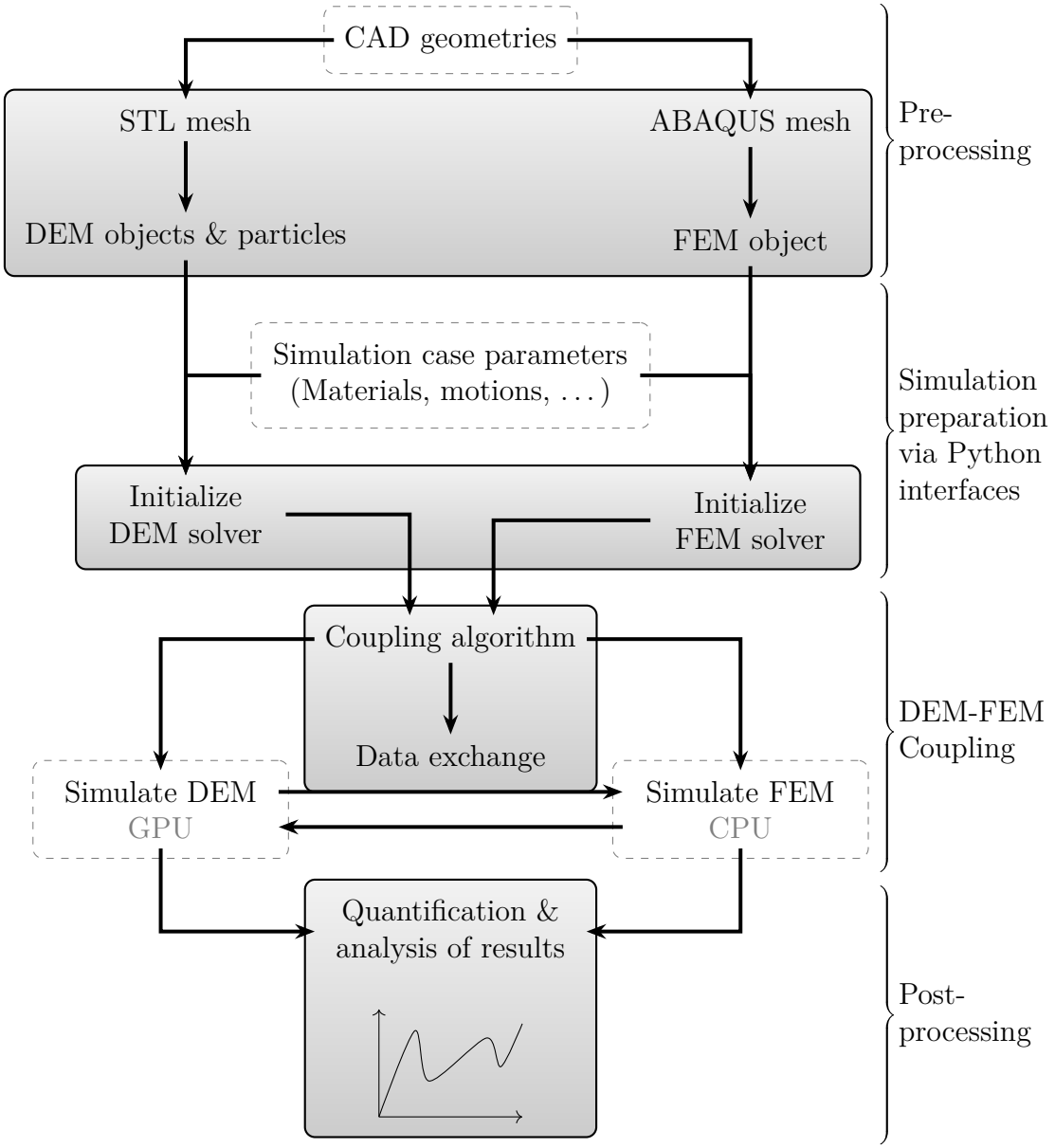

Figure 3.2: Workflow for a case-specific coupled simulation. The steps performed as contribution within this thesis are highlighted as gray boxes. Steps that are covered externally are highlighted as white boxes with a dashed border.

meant for the FEM simulation describing the FEM object is converted to a shell or volume element mesh saved as an ABAQUS file. These files are then used in the next step during the initialization to create the objects and particles in the corresponding simulation environments.

The DEM and FEM solver are initialized via their Python interfaces during the stage of simulation preparation. Another input besides the object and particle geometries are the case specific simulation parameters that specify for instance material characteristics, object motions or timestep sizes.

The actual simulation of the case is then performed by the coupling algorithm that was described in detail through this section. During the coupling algorithm, the DEM solver is called via the Python interface and simulates n^D simulation steps in C++ on the GPU utilizing CUDA. Similarly, the FEM solver is called via its Python interface and performs a simulation step in C++ on the CPU. During each coupling algorithm iteration, data is exchanged between the solvers covering the force boundary condition and object movement update.

Finally, for each simulation case post-processing is performed. Already during the coupling simulation, quantities of interest are computed, gathered and saved in a CSV file. Examples of quantities of interest are the mass flow rate of particles, the deflection of a FEM object or particle and object velocities and the list of quantities of interest varies between different simulation cases. After completing a simulation, the saved data is analyzed and visualized as animations or plots.

4

Beam with fixed ends under constant load

In the previous chapter, we presented the formulation of the coupling algorithm. The natural next step is to verify and validate our model. As a first verification, we choose a case with a small amount of particles and a small-scale deflection to focus on the data transfer of the interaction. More precisely, we simulate the case of a fixed beam under constant load as presented by Dratt and Katterfeld [26]. Further verification and validation against experimental data will be presented in a later chapter.

4.1 Configuration and material specifications

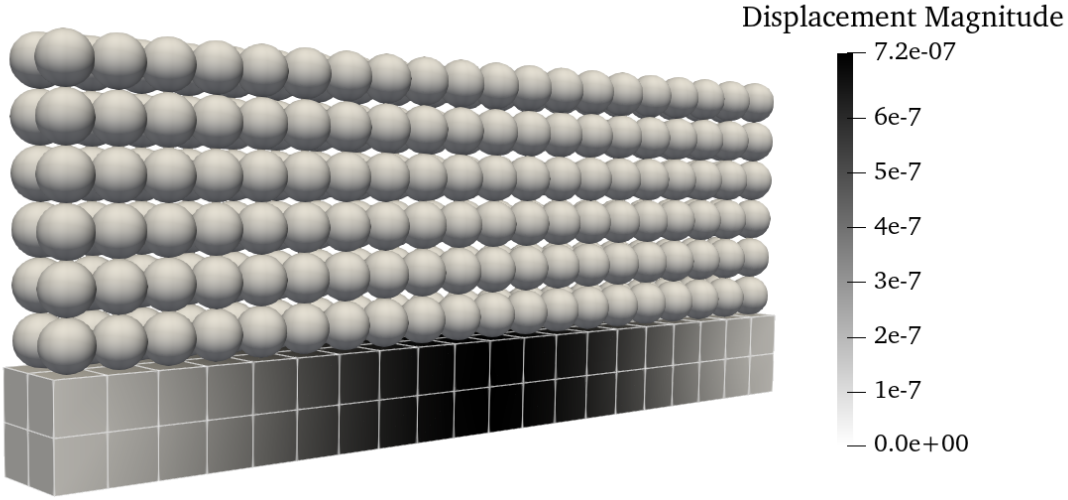

Figure 4.1: Visualization of the deflection of a beam with fixed ends under constant uniformly distributed load.

A set of spheres lie on top of a beam, as visualized in Figure 4.3. The spheres apply a constant, approximately uniformly distributed load, causing a displacement with its maximum at the center of the beam. The dimensions of the beam and the material parameters are listed in Table 4.1. The beam has dimensions of $1,000 \times 100 \times 100$ mm (L×W×H) and is discretized with an element size of 50 mm and simulated with

Description	Value	Unit
Length	1,000	[mm]
Width	100	[mm]
Height	100	[mm]
Young's modulus	210	[GPa]
Poisson's ratio	0.3	
Density	7,800	[kg/m^3]

Table 4.1: Dimensions and material parameters of the simulated beam based on the specifications of Dratt and Katterfeld [26].

material properties corresponding to mild steel. The total mass of the spheres is 51 kg which results in a pressure of 0.005 $\frac{\mathrm{N}}{\mathrm{mm}^2}$ on the upper surface of the beam.

4.2 Analytical solution for beam deflection

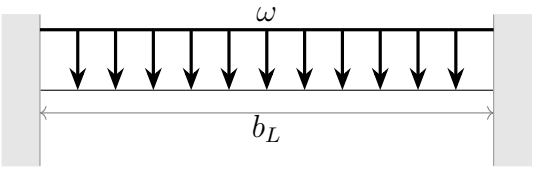

Figure 4.2: Illustration of a beam with length b_L under a constant uniformly distributed load ω fixed at both ends.

In order to give an understanding of the maximal deflection, let us give the analytical formula. First of all, we need to compute the pressure acting on the beam, depending on the load mass and gravity. In this case, let us denote the total load mass as m, the gravitational constant by g_c and the length and width of the beam as b_L, b_W, respectively. Then, the pressure of the load P is given by

$$P = \frac{mg_c}{b_L b_W}. \tag{4.1}$$

Following Budynas, Nisbett, et al. [55], let us denote the beam's Young's modulus as E and the length, width and height of the beam as b_L, b_W, b_H, respectively. Then, the second moment of area I is

$$I = \frac{1}{12} b_W b_H^3 \tag{4.2}$$

and the distributed load $\omega = P \cdot b_W$. Finally, the maximal deflection δ_{max} of the beam is computed as follows:

$$\delta_{max} = -\frac{\omega b_L^4}{384EI}. \tag{4.3}$$

Given the analytical solution, we can derive the maximal deflection of the beam for a constant load of 51 kg and analogously for other loads. With a pressure of 5,000 $\frac{\mathrm{N}}{\mathrm{m}^2}$ and a beam width of 0.1 m, the resulting uniform load is

$$\omega = 500 \ \frac{\mathrm{N}}{\mathrm{m}}. \tag{4.4}$$

The 2nd moment of area I in this case is

$$I = \frac{1}{120{,}000} \ \mathrm{m}^4 \tag{4.5}$$

as the beam has a width and height of 0.1 m. The modulus of elasticity for mild steel is 210 GPa and hence the resulting maximal deflection of the beam with 1 m length is

$$\delta_0 = -7.4 \times 10^{-7} \ \mathrm{m}. \tag{4.6}$$

4.3 One-way coupling with quasi-static FEM

In this example we use a one-way coupling as the effect of the beam's deflection on the spheres is neglectable considering the size relation of the spheres to the maximal deflection. As the load is constantly acting on the beam, this case is elastostatic and thus, we use the static FEM solver to simulate the beam. Hence, we first simulate some seconds with DEM to ensure that the spheres reach a steady-state, transfer the acting forces on the beam to the FEM solver and then solve with FEM until we find a solution.

4.4 Simulation results of beam deflection

The simulation results of the fixed beam under constant load are summarized in Table 4.2 for two different masses, namely 51 kg and 72 kg. The simulations were repeated 20 times, but the results showed no statistical variation, as expected for this static case.

		Error		
	Deflection [m]	**Absolute** [m]	**Relative**	**Mass** [kg]
Pure FEM	-7.06×10^{-7}	-	-	51
Coupling	-7.04×10^{-7}	2.74×10^{-9}	0.38	51
Pure FEM	-9.97×10^{-7}	-	-	72
Coupling	-9.89×10^{-7}	8.52×10^{-9}	0.85	72

Table 4.2: Collection of deflection of pure FEM and coupled solution for a load of 51 kg and 72 kg and corresponding absolute and relative error from coupling results to the finite element solution for the case of a beam with both ends fixed under a constant load and an element size of 50 mm.

As a reference for the computation of the error in the beam deflection we refer to the finite element solution. This choice was done as the finite element solution converges to a value only close to the analytical solution and the coupling can only be expected to be as close as the finite element solution.

Dratt and Katterfeld [26] achieved a relative error of less than 1% for a mass of 51 kg for an element size of 50 mm with their simulations. The here presented coupled solution delivers similarly a relative error of less than 1% compared to the pure FEM solution for all of the chosen mesh resolutions. In more detail, the coupled solution has a relative error of 0.38 % as compared to the pure FEM solution for a mesh element size of 50 mm.

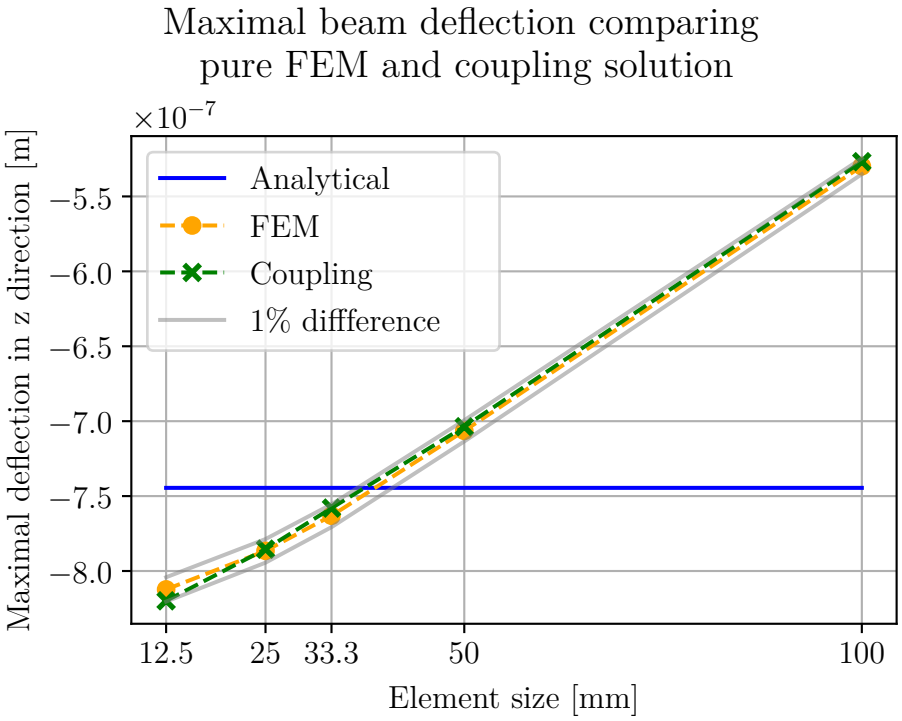

Figure 4.3: Plot of resulting maximal deflections of analytical, pure FEM and coupling solution for different mesh resolutions and a load of 51 kg.

Comparing in general the analytical and the pure FEM solution, one can see that they are close to each other. Furthermore, from the behavior of the maximal deflection for finer meshes as visible in Figure 4.3, one can conclude that the finite element solution for the desired case of 51 kg converges to a value lower than the analytical one.

In summary, the results of this simulation case show that the load from DEM particles to the FEM object is correctly transferred within the coupling algorithm.

5

Deformation of fixed steel sheet under material flow

For the validation of our model we choose to replicate the experiment of a fixed steel sheet under a material flow. With this case we investigate the correctness of the coupling algorithm for dynamic interactions between particles and objects.

5.1 Experiment description

As a reference for comparison, we rebuild the experiment performed by Dratt and Katterfeld [26]. In the experiment, the upper chamber (the top see-through container in Figure 5.1) is filled with wheat grains until a total mass of 6 kg is reached. The bottom of the chamber consists of two hand-slides. The positions of the hand-slides can be adjusted such that an outlet of a certain length occurs between them. During the experiment the wheat grains fall through this outlet into the lower chamber. A flap system is installed beneath the hand-slides which opens within 0.2 s at the beginning of the experiment. As the flap system is located beneath the hand-slides with a gap, there are particles, collecting and forming an initial bulk. Beneath the upper chamber, there is the lower chamber (the bottom see-through container in Figure 5.1) containing a frame that holds a thin steel sheet. The steel sheet is fixed on its left side as illustrated in Figure 5.1. Once, the experiment starts, the flap system opens, letting the initial bulk fall down and more particles are following through the opening created by the hand-slides. Thus, there is a continuous (but not necessarily constant) material flow until the upper chamber is mostly emptied. Under the load of the material flow, the steel sheet deflects as visualized in Figure 5.1. In the experiment, a distance sensor was installed beneath the steel sheet, allowing the deflection to be measured.

We replicate the experiment virtually with simulations with the same setup and track approximately the same position of the steel sheet to measure its deflection.

5.2 Simulation parameter specifications

The bulk density and porosity of wheat are given and summarized in Table 5.1. Using this information we can deduce the material density needed in the DEM solver. The particle density ρ_p is then 1.2×10^3 kg/m^3. The particle diameters

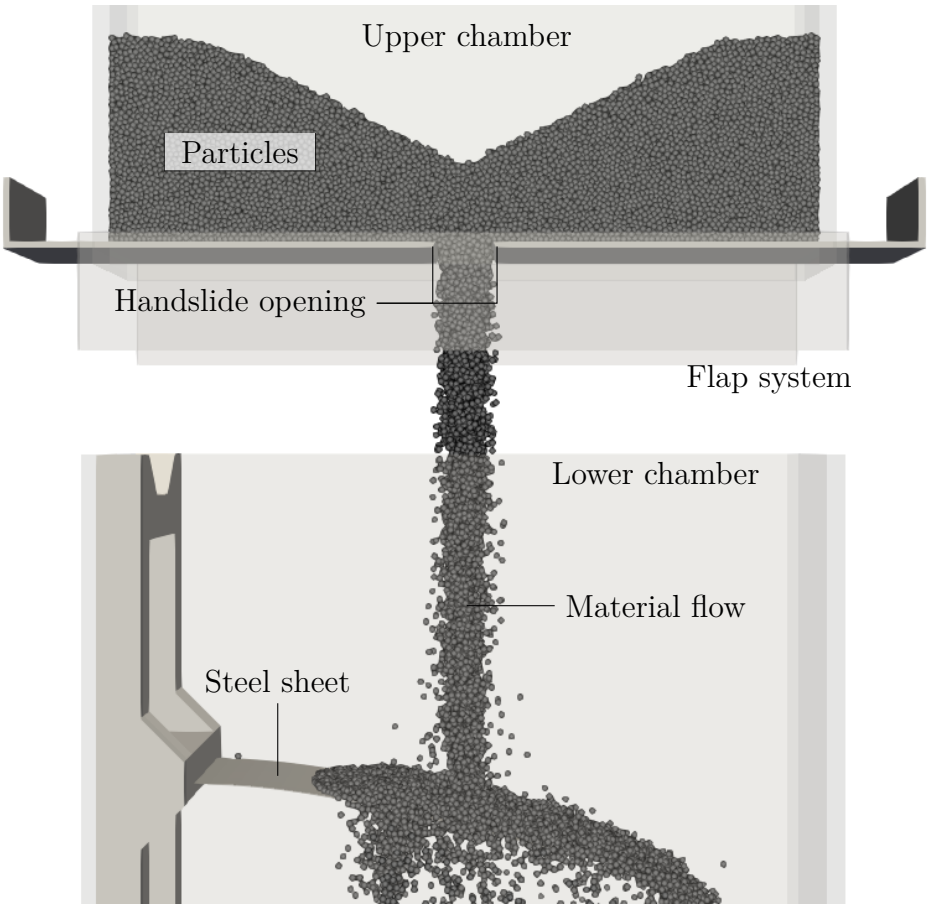

Figure 5.1: Simulation snapshot of the deflecting steel sheet under material flow of particles with a spherical shape. The nomenclature of the case description is added as annotations.

are distributed uniformly in the range $[3, 5]$ mm. The simulation starts with the generation of a total mass of 6 kg of wheat particles inside the upper chamber. In our simulations that results in approximately 164,000 wheat particles.

The particles are inserted into the simulation randomly within the whole volume of the upper chamber. They are then arranged on the bottom of the upper chamber by the gravitational force. During particle generation the total mass is tracked and the insertion is completed as soon as a total mass of 6 kg is reached. We let the simulation continue for another short time period to ensure that the particles have fallen down and reached a steady state. We save the state of the particles and access it for all later simulations.

In Table 5.1 we summarize all parameters stated in [26]. We use the same parameters as in the experiment as a starting point, but as described in later sections, we also calibrate our model, which leads to some differences. Furthermore, we state additional parameters in Table 5.2 that we need to specify in our simulation setup.

Property	Value	Unit
Bulk density ρ_b	743	kg/m^3
Porosity ϵ	0.4	
Size distribution	[3,5]	mm
Particle-steel friction coefficient	0.22	
Particle-frame friction coefficient	0.26	
Total bulk material mass	6	kg
Coulomb friction	0.17	
Particle Young's modulus	100	MPa
Particle Poisson's ratio	0.3	
Falling height	360	mm
Outlet length	40	mm
Measurement position	60	mm
Flap opening duration	0.2	s
Thickness steel sheet	0.75	mm
Dimensions (L×W) steel sheet	340 × 100	mm
Area (L×W) of clamp boundary on steel sheet	60 × 100	mm
Steel Young's modulus	185	GPa
Steel Poisson's ratio	0.3	
Steel material density	7,850	kg/m^3
Element edge length	10	mm

Table 5.1: Collection of simulation parameters based on the values given by [26].

Property	Value	Unit
Particle density ρ_p	1,242	kg/m^3
Particle restitution	0.4	
Gap size	12	mm
Frame density	7,800	kg/m^3
Frame Young's modulus	100	MPa
Frame Poisson's ratio	0.3	

Table 5.2: Additional simulation parameters used in this thesis.

5.3 Simulation calibration to reach experimental angle of repose and mass flow

We need to calibrate our model to approximate the experimental results. There are two key values for calibration given:

- Angle of repose of 26°.
- Mass flow rate which is described for the experiment, but not explicitly given.

Note that the focus for calibration lies on the DEM simulation as both values mentioned above are dependent on the particle material, the amount of particles and

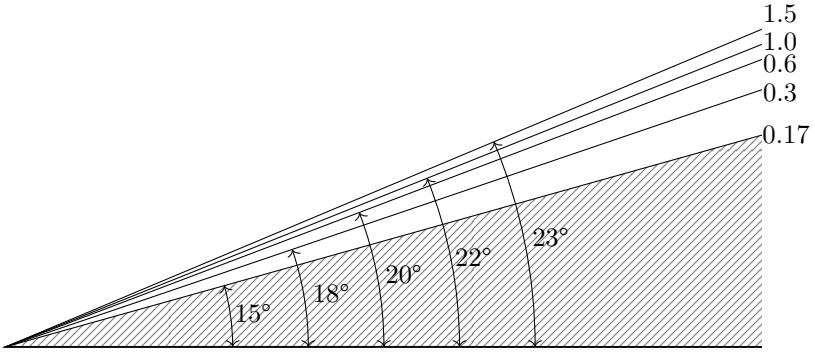

Figure 5.2: Angle of repose visualization for different Coulomb frictions. The hatched area represents the final particle pile in the upper chamber for a Coulomb friction of 0.17 as was reported in the experimental results. The different resulting angles for Coulomb frictions of $\{0.17, 0.3, 0.6, 1.0, 1.5\}$ are shown.

the initial bulk reservoir between hand-slides and flaps.

The Coulomb friction of the particle-particle interaction is a significant parameter for the angle of repose. With the initial friction of 0.17 as stated in the original paper, we only achieve an angle of repose of 15° which is lower than given in the experiment description. Increasing the friction results in an increased angle of repose although the increase flattens fast and converges to a value around 23°, as visible in Figure 5.2. Thus, we simulate with a friction of 1.0 which results in an angle of repose of 22° in our simulations.

Potentially a lower friction value could have been applied if the effect of rolling friction was separately considered. That was not the case in the current simulations.

In the report of the original experiment, a description of the mass flow rate over time is available. The main points are summarized here:

- Around $t = 0.25$ s the initial mass flow rate is significantly higher than at later points due to an initial bulk material reservoir in gap between hand-slides and flaps.
- At $t = 0.42$ s the mass flow rate is reduced suddenly as the initial reservoir has fallen down and the flow stabilizes.
- During the time interval $t \in [0.5, 1.5]$ s the mass flow rate is constant.
- After $t = 2.0$ s the mass flow rate reduces until $t = 4.5$ s as at this time most of the material has fallen out of the upper chamber.

It is clear from the description, as well as the numerical studies performed for this thesis, that the gap between hand-slides and flaps has a significant influence on the achieved mass flow rate. As the gap size is not stated in the experimental setup description, a parameter study is necessary to see which gap size approximates the peak in the deflection of the steel sheet best. The result of such a parameter study can be seen in Figure 5.3, where the mass flow rate over time for the coupled simulation is visualized. The mass flow rate is measured for a gap size of 12 mm, at the bottom of the flap system.

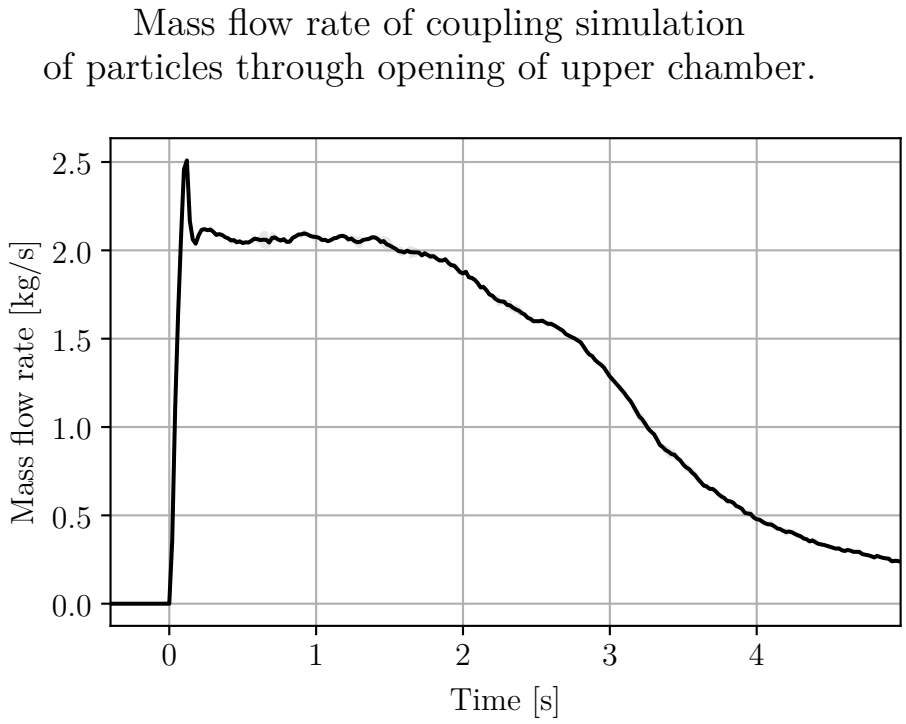

Figure 5.3: Mass flow rate of the coupled simulation for a calibrated gap size of 12 mm between hand-slides and flaps for spherical particles.

As we measure the mass flow rate directly beneath the flap system, the characteristic points appear earlier in our mass flow rate result than in the description from the experimental one. The mass flow rate is - as explained in subsection 2.1.4 - measured during a time interval and the interval length also influences on the mass flow rate responds to changes in the mass flow.

Considering the four significant intervals as stated above, our resulting mass flow rate depicts a qualitative replication of the description. In the beginning around $t = 0.25$ s our initial mass flow rate has a peak, meaning that it is significantly higher than directly after that due to the initial particle bulk. The mass flow rate drops then suddenly at $t = 0.3$ s as the initial bulk has fallen down. In the interval of $t \in [0.3, 1.5]$ s the mass flow rate stabilizes and is roughly constant. Then, in the final stage, the mass flow rate reduces further in a non-linear manner until most of the material has fallen out at the end of the simulation.

5.4 Investigation of convergence and stability of the dynamic coupling

We model the thin steel sheet with shell elements and use a transient time integration for the FEM simulation of it, as this case is of dynamic nature. Early investigations of the simulation showed that the current case is more demanding for the coupling algorithm and prone to instabilities for poorly chosen simulation parameters. A

symptom of such instabilities were extreme forces acting on the steel sheet that result in extreme deformations. The integration methods in the applied solvers differ, but both are methods of at least first order. Thus, the choice of timestep in both methods has influence on the accuracy. For relatively large timesteps as in this simulation case, the results of the integration methods differ between the two solvers such that the meshes are drifting slightly apart. The correction done in each coupling timestep of the positions of the triangle mesh caused these extreme forces, as suddenly many particles overlapped with the mesh.

To keep the position of the coupled flexible object aligned between both solvers, we introduce numerical damping in the FEM simulation to dampen the accelerations. As suggested in Wood, Bossak, and Zienkiewicz [54], we apply the Bossak-Newmark damping method with parameters $\alpha = 0.1, \beta = 0.3$ and $\gamma = 0.6$ to the FEM simulation and achieve stable coupling results for a FEM timestep $\Delta t^F \leq 10^{-4}$ s.

As mentioned in section 2.1, the timestep must be chosen sufficiently small such that the theory of DEM is applicable. In subsection 2.1.5 we introduced a measure - the Rayleigh timestep - that can be seen as an upper bound of the DEM timestep. Experiments showed that we need to choose the DEM timestep $\Delta t^D \leq 10^{-5}$ s to achieve a stable DEM solution. Furthermore, we investigated if the solution is converging further for smaller DEM timesteps, but it had no effect. As in this case a maximal velocity of 3 m/s is achieved and the minimal particle radius is 3 mm, we can deduce from Figure 2.5 that 10^{-5} s is a suitable timestep choice and that the error should reduce for even smaller timesteps, but that a reduced error on this scale might not give significant improvements on the simulation results.

We also studied other parameters, such as the mesh refinement and the Newmark parameters, to further investigate the convergence and stability of our simulations. But besides the introduction of damping and the FEM timestep, the other tested parameters had no significant influence on the convergence or stability.

5.5 Simulation results of steel sheet deflection under material flow

In Figure 5.4 a comparison of the steel sheet deflection between the experiment and the coupling simulations for spherical particles is displayed. The peak of the curve representing the axial deflection, when the mass flow is the highest, is matched by our simulation. The abrupt back-bending of the steel sheet after the peak is also approximated closely by the simulation. Furthermore, the steady-state period of the deflection and the mass flow is depicted in our result. Only in the reducing material flow, our results show a slightly different behavior in the deflection as the back-bending happens delayed.

In conclusion, we match the original experiment well with the simulation as the most significant key points are reproduced with qualitative and quantitative satisfactory results.

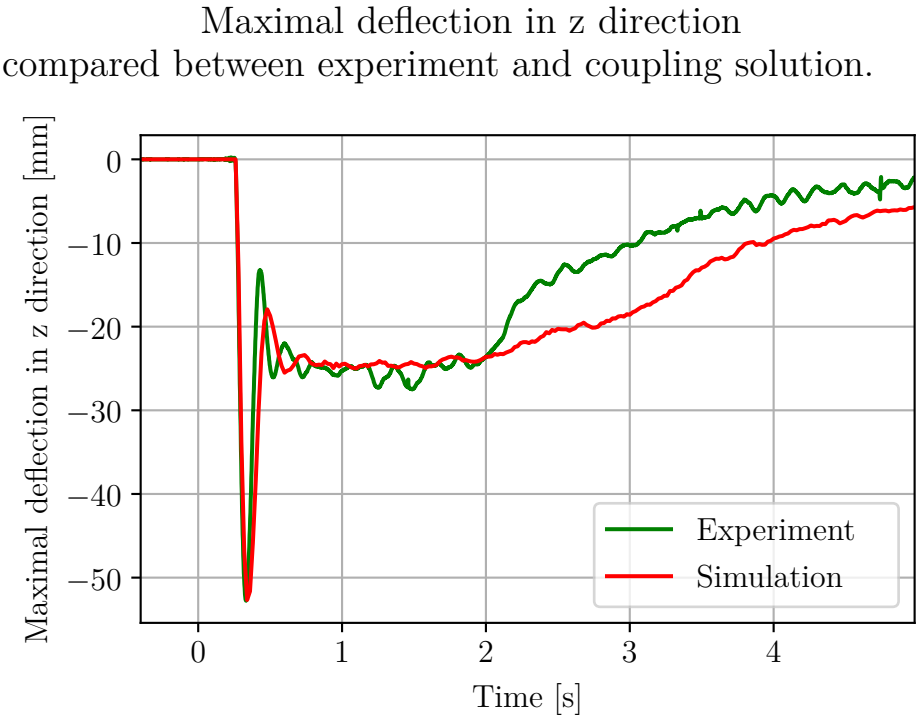

Figure 5.4: Deflection of the steel sheet compared between the experiment of the referenced paper (green) and the coupled simulation (red) for spherical particles.

5.6 Performance measurements

The coupling algorithm is based on an existing implementation of Demify® and LaStFEM. Within the coupling algorithm few operations are performed in comparison to the solvers, since we only transfer data and have no system of equations to solve. Thus, we expect that the solvers account for a majority of the simulation time. One aim for the performance of the coupling algorithm itself is that it takes less time than each of the solvers.

In Table 5.3 the time measurements of the coupling algorithm applied on the steel sheet under material flow are shown. The time measurement was performed on a machine with a Xeon Gold 6134 CPU with a clock speed of 3.20 GHz, 8 cores and 192 GB of memory as well as a V100 GPU with 32 GB of memory. With 77 %,

Total time	DEM	FEM	Coupling
116	89 (77 %)	21 (18 %)	6 (5 %)

Table 5.3: Performance measurement in minutes of the total time of the coupling algorithm, separated in the pure DEM simulation, the pure FEM simulation and operations specific for the coupling. The performance is measured for 86,000 particles and 340 elements in the object discretization. The results are a mean computed over 10 repetitions.

the DEM simulation accounts for most of the total time. The time consumed by the FEM simulation is 18 % of the total time. As we have more than 200 times more particles than FEM elements, the number of degrees of freedom of the DEM simulation outweighs the number of degrees of freedom of the FEM simulation. Additionally, the DEM timestep is two powers smaller than the FEM timestep, wherefore DEM solves for the degrees of freedom more often. Thus, it is justified that DEM accounts for a majority of the time. In a simulation with the same number of degrees of freedom we expect the FEM simulation to account for the majority of the time as in contrast to DEM the equation system to solve is of a more implicit nature. All coupling operations together have a simulation time of 5 %, which is the shortest part of the simulation.

6

Simulation of interaction between a sleeper and a ballast bed

In section 1.2, we saw that DEM-FEM coupled simulations have been previously applied for the simulation of railroad, specifically the interaction between ballast material and sleeper. With the goal of developing a coupling algorithm for infrastructure simulations, we replicate the setup of the experiment by Song et al. [31]. Furthermore, we extend the simulation case to investigate the effects of different simulation parameters, such as material properties, on the simulation results. Additionally, we investigate railroad simulation for complex shaped particles instead of spherical particles.

6.1 Experiment description

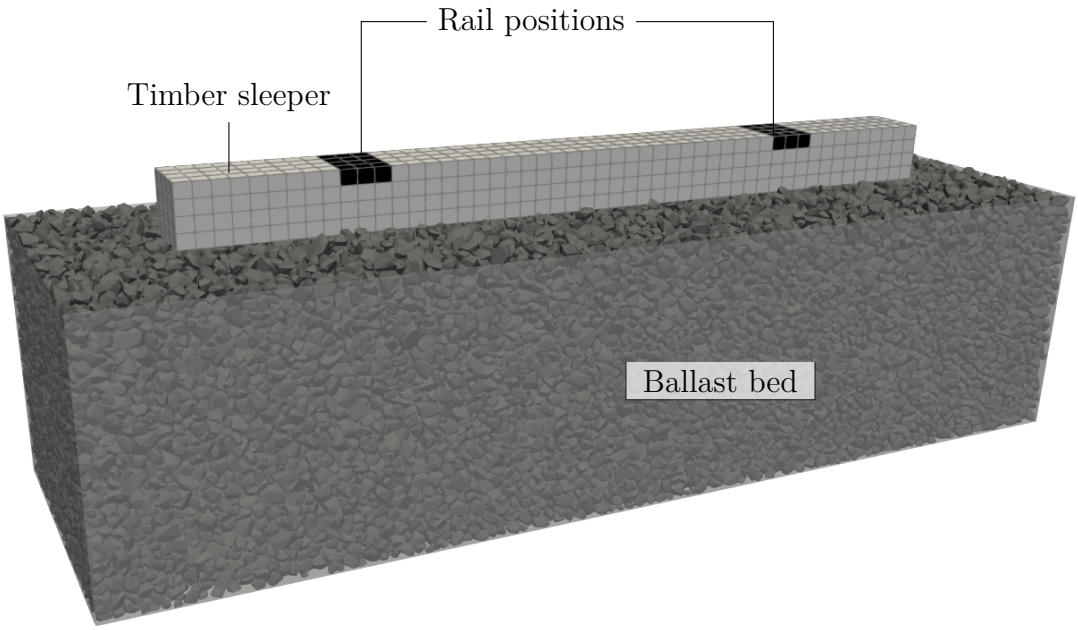

Figure 6.1: Visualization of a timber sleeper on top of rock particles inside a ballast bed. The rail positions on the sleeper are highlighted in black.

In the laboratory experiments performed by Song et al. [31], a bed with dimensions 3.2 × 1.0 × 0.8 m (L×W×H) was filled with railroad ballast material. After a vibratory compaction, 5 pressure cells were placed at a depth of 0.13 m to measure the pressure distribution within the ballast bed. Then, the ballast bed was leveled.

In the experiment the interaction for both steel and timber sleepers were investigated. Within this thesis we constrain the simulations to timber sleepers. In the experiment a timber sleeper with dimensions 2.5 × 0.2 × 0.18 m (L×W×H) was positioned on top of the ballast bed as visualized in Figure 6.1. A load was applied onto the sleeper at both rail positions following a prescribed pattern. An accelerated version of the loading pattern with a lower maximal load that is applied in the simulations is visualized in Figure 6.2. First, an increasing load from 0 to 220 kN is applied, then a cyclic loading ranging from 4.4 to 44 kN with a frequency of 2 Hz and finally the same increasing load as in the first step is applied. The pressure distribution within the ballast bed given by the sensor measurements is then evaluated for different load levels. The load levels that we compare to are 44 and 132 kN of the linear loading stage, both before and after cyclic loading.

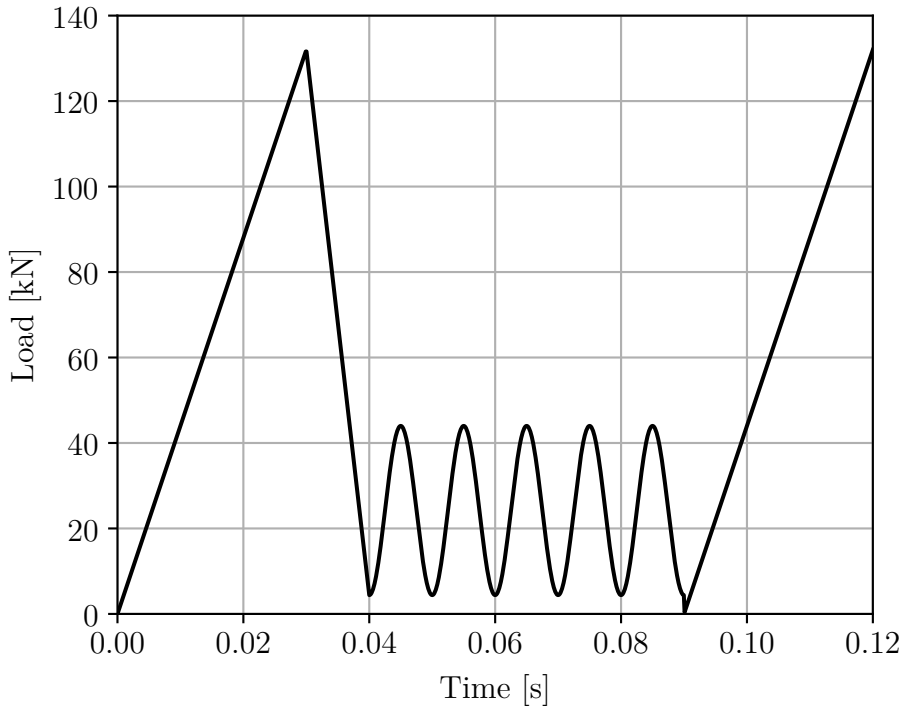

Figure 6.2: Loading pattern for railroad simulation based on Song et al. [31].

6.2 Simulation specifications

In the simulations we replicate the box holding a particle bed with a timber sleeper on top. As the experiment was performed with rock-shaped particles, we choose the dilated polyhedron model to simulate them. We investigate the results for two different distributions of the characteristic particle size.

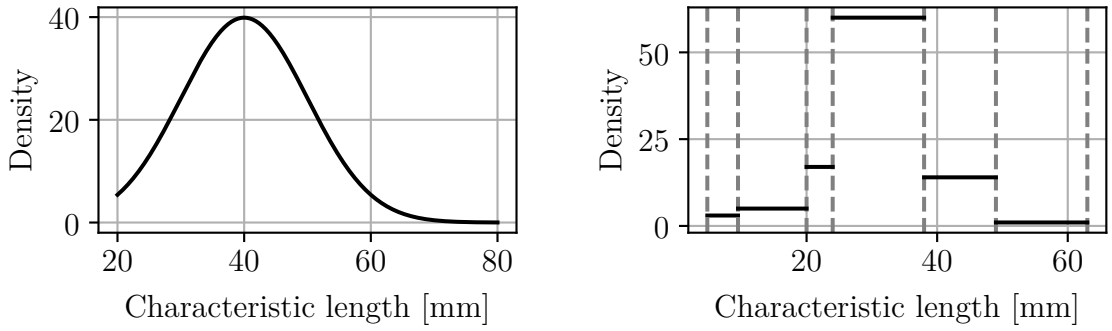

(a) Normal distribution **(b)** Piece-wise constant distribution

Figure 6.3: Visualizations of a normal (a) and piece-wise constant (b) distributed characteristic length of rock particles in a particle population.

The first size distribution is a normal distribution with mean 0.04 m and a standard deviation of 0.01 m. Minimal and maximal sizes are given as 0.02 and 0.08 m, respectively. The normal distribution is specified as to give a similar number of particles as used for simulations on the system reported by Song et al. [31].

A second size distribution was used for the simulations with a distribution more closely to the ballast aggregate gradation as presented for the experiments by Song et al. [31], namely a piece-wise constant distribution as presented in Figure 6.3. Due to the algorithm of the dilated polyhedron model, we restricted the lower bound of the piece-wise constant distribution to 0.02 instead of 0.0048 m. The dilated polyhedron model applied imposes a lower limit on the dilation radius under high load conditions.

The process of creating the numerical experiment with a compacted particle bed, sensors and the sleeper in place consists of several steps. The main steps are outlined in Figure 6.4 as to give a better understanding of the simulation setup.

First, the rock particles are generated with the given size distributions and a dilation radius r_{ds} corresponding to 10 % of the characteristic length and, after generation, compaction is applied. After the first generation and compaction, all particles with a mass center above 0.57 m are removed in order to place the pressure sensors in the correct position.

Second, sensors represented by cuboid objects with a dimension of $0.22 \times 0.22 \times 0.1$ m are placed equidistantly on the bed. The middle sensor is positioned at the center of the sleeper at an x coordinate of 1.6 m. The other four sensors are then placed relative to the center one with a distance of 0.38 m to each other. This way, the pressure can be measured at a depth of 0.13 m. After the sensors are positioned, particles are generated again, compacted with a sinusoidal compaction pattern and all the particles with a mass center above 0.8 m are removed. Note, that the sensors are considered rigid objects and simulated purely with the DEM solver and a dynamic motion corresponding to the forces from the surrounding particles.

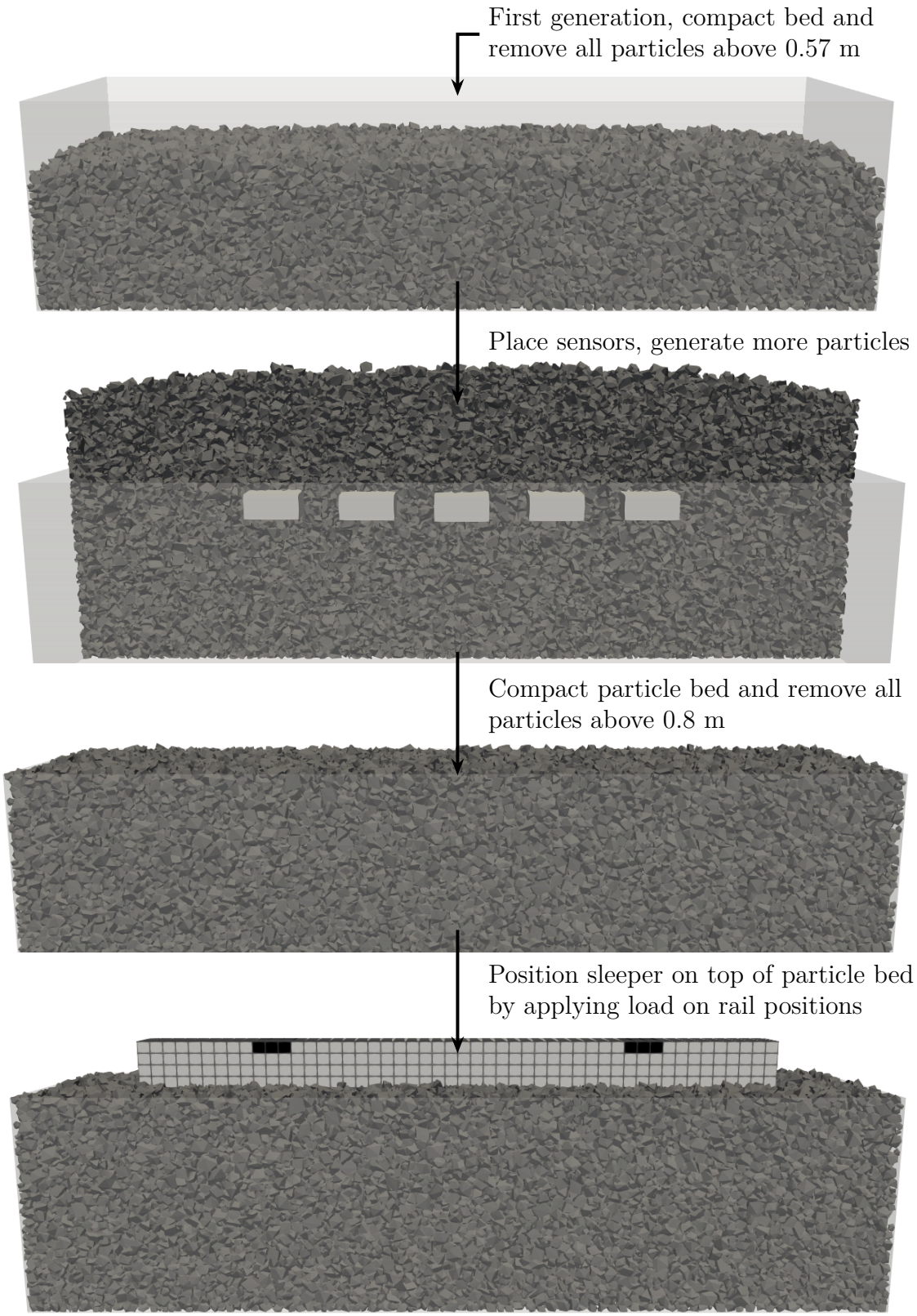

Figure 6.4: Visualization of generation process of a simulation state.

Property	Value	Unit
DEM timestep Δt^D	10^{-6}	s
FEM timestep Δt^F	10^{-3}	s
Particle density ρ_p	2,600	kg/m^3
Particle-particle friction coefficient	0.6	
Particle Young's modulus	10	GPa
Particle Poisson's ratio	0.27	
Particle restitution	0.2	
Sleeper density	800	kg/m^3
Sleeper Young's modulus	9	GPa
Sleeper dimensions (L×W×H)	$2.5 \times 0.2 \times 0.18$	m
Horizontal rail positions on sleeper	$[0.8825, 2.3175]$	m
Rail dimensions (L×W)	0.15×0.2	m
Ballast bed dimensions (L×W×H)	$3.2 \times 1.0 \times 0.8$	m
Sensor dimensions (L×W×H)	$0.22 \times 0.22 \times 0.1$	m
Sensor distances	0.38	m

Table 6.1: Simulation parameters for the case of a timber sleeper under dynamic loading as in [31].

Then, the timber sleeper is created above the particle bed and a first light load of 100 N is applied onto the sleeper to position it. Once the sleeper has settled on the particle bed, the loading cycle starts as given in Figure 6.2 and is applied as pressure boundary conditions at the positions of the rails onto the sleeper. The sleeper is simulated with FEM.

6.3 Stability

As this is the first coupled simulation with complex shaped particles in this thesis, a new investigation of the stability is required. For the particle shapes we use scans of actual convex rocks to create a dilated polyhedron particle model.

A reasonable balance between the dilation radius and the elasticity of the particles is required for the DEM simulation to be stable. In general, the smaller the dilation radius, the higher modulus of elasticity is required to avoid too large overlaps. We found that as a rule of thumb, a dilation radius of 10 % of the characteristic length together with a modulus of elasticity of 10 GPa established valid contacts for this case.

In a first draft, our simulations of the sleeper-ballast interaction with the coupling algorithm revealed instabilities leading to too large reaction forces and thus unphysical behavior of the sleeper. To increase the number of contacts of the sleeper itself with the particle bed, we implemented a compaction scheme. A large plate object moves with a sinus wave as visualized in Figure 6.5 from above down onto the particle bed. With this movement, the particle bed is compacted and a more even upper surface is created offering more points of contact when interacting with the sleeper.

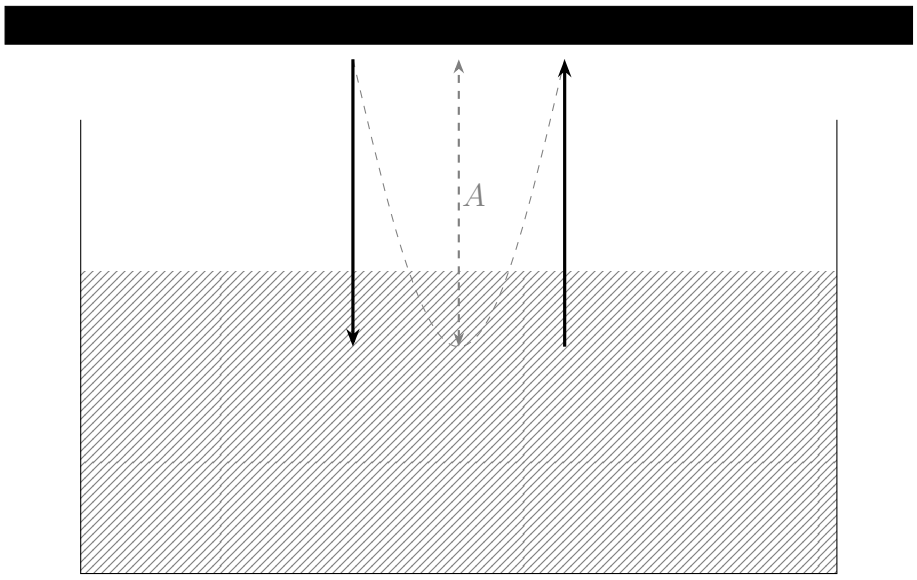

Figure 6.5: Visualization of the compaction method for the ballast bed with a large plane geometry moving from above down onto the particle bed with a sinus wave movement pattern with amplitude A.

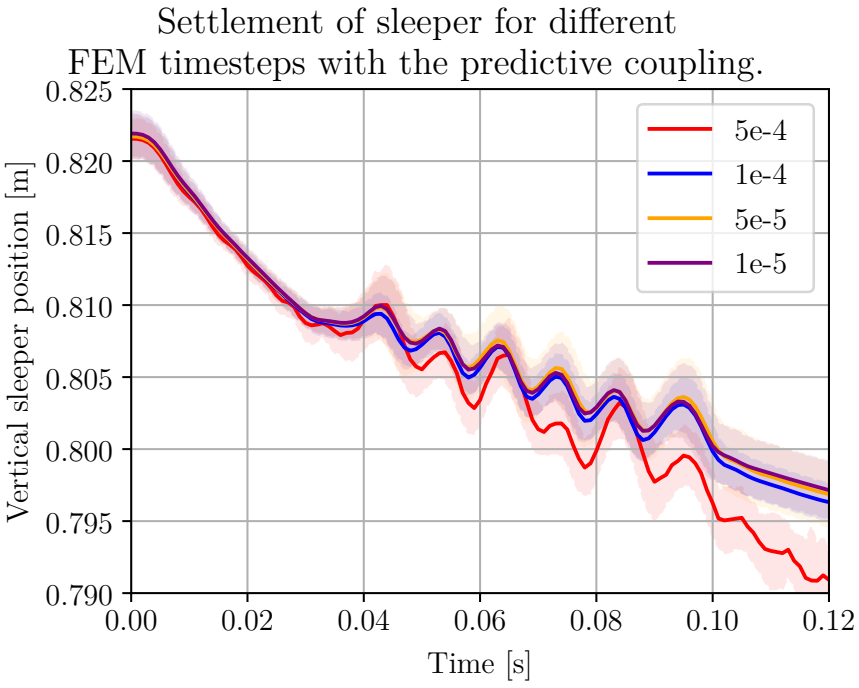

Figure 6.6: Vertical position of sleeper representing its settlement for different FEM timesteps with the predictive coupling scheme.

In the experiment, a vibratory compactor is applied for compaction.

Further parameters connected to the stability for this case is the FEM and DEM timesteps, Δt^F and Δt^D respectively. In the early tests, we used similar timestep settings as was applied for the steel sheet case in chapter 5, i.e. $\Delta t^D = 10^{-5}$ s

and $\Delta t^F = 10^{-3}$ s. The motivation was that this simulation case is of a much less dynamic nature than the steel sheet. However, the forces acting between ballast and sleeper are high, requiring a smaller timestep to resolve the contacts properly. Thus, a DEM timestep $\Delta t^D \leq 10^{-6}$ s is necessary. Additionally, a FEM timestep $\Delta t^F \leq 10^{-5}$ s is required for stability with the just-in-time coupling as for long timesteps instabilities in the forces occured. A reason for the need of a smaller timestep than for the steel sheet might be that the loading pattern applies high forces that may be more extreme than the incoming material flow onto the steel sheet.

However, for the predictive coupling the FEM timestep can be increased to 10^{-4} s. In Figure 6.6 we visualize the sleeper settlement for different FEM timesteps for the predictive coupling. It is unstable for a timestep of 5×10^{-4} s, but for all timesteps $\Delta t^F \leq 10^{-4}$ s the simulation behaves similarly and stable. The increased stability of the predictive coupling is expected as we predict the velocities such that the object position during the coupling update is always the same between DEM and FEM domain.

6.4 Parameter studies

In contrast to the simulations presented in chapter 5, there are no calibration quantities besides the final pressure distribution to be compared to the experimental results. Thus, we study a selection of parameters and their effect on the mentioned pressure distributions. To further quantify the influence of different parameters, we measure the effect as the settlement of the sleeper as its position in vertical direction as well as the maximal strain for all sleeper elements. Note that all visualizations of simulation quantities display the mean over 10 repetitions with the standard deviation as pale band around the mean.

6.4.1 Time scale of loading pattern

The loading pattern in Figure 6.2 is an accelerated version of the one applied in the experiment, i.e. 50 times faster. The acceleration was performed in order to shorten the simulations. However, it should be numerically evaluated that speeding up the loading pattern does not alter the conditions of the experiment. Thus, we study the time scale to investigate the effect of the acceleration. This parameter specifies the scaling in time of the loading pattern. For instance, with a time scale of 2.0 the loading pattern is stretched to last 0.24 s instead of 0.12 s as for time scale 1.0.

In Figure 6.7 we present the settlement of the sleeper for time scales of $1.0, 2.0, 10.0$ and 20.0. We stated earlier that the particle bed has a height of 0.8 m. In the plot however, the sleeper starts with a vertical position of its bottom surface at 0.82 m. This is due to the fact, that after the generation and compaction of the particle bed, we remove all particles with a mass center above 0.8 m. Parts of particles then might still be above the mentioned axial position as their mass center lies below. When then positioning the sleeper, we place it with a first light load onto the particle bed and with this possibly on top of those particles which stick out.

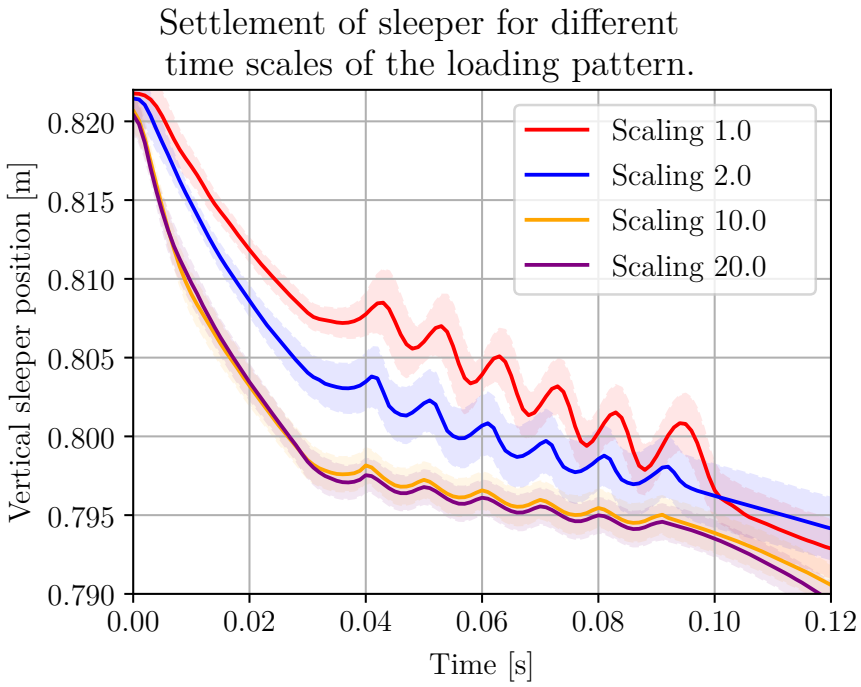

Figure 6.7: Vertical position of sleeper representing its settlement for different time scales. On the x axis the reference time for a scaling of 1.0 is given.

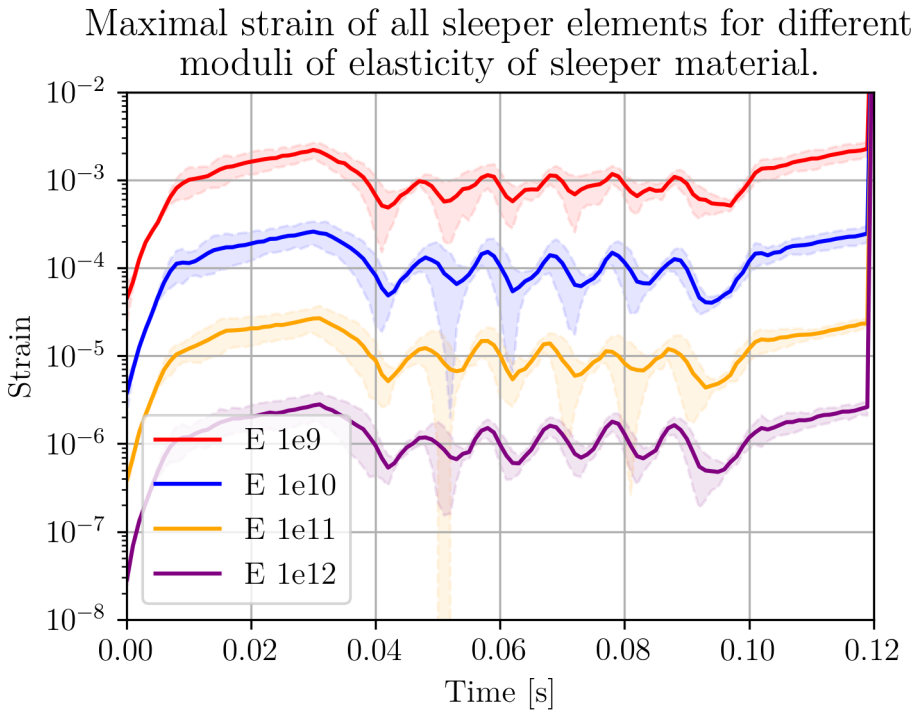

Figure 6.8: Maximal strain of all sleeper elements for different moduli of elasticity of the sleeper material.

A difference in our results is clearly visible for the different time scales. The standard deviation gets smaller for a larger time scale indicating a statistical reliability of the simulation. Similarly, the amplitude of the position change during the cyclic loading (reference time $0.03-0.09$) is lower and less varying for longer time scales. For a time scale of 1.0 the amplitudes are noticeably different from cycle to cycle. Accelerating a movement, can alter the physical characteristics of a case. Here, the results suggest that with the accelerated movement the pressure is applied too fast on the sleeper to maintain the inertia of the experiment. This suggests that the speed-up load cycle leads to inertial affects in the bed and thus is not a valid approximation in comparison to the experimental setup. However, the results for a time scale of 10.0 and 20.0 are similar, which indicates a convergence for increasing time scales. To save computational time for the results presented further in the thesis, we conclude that a time scale of 10.0 is sufficiently close to the expected limit for the original time scale of 50.0.

6.4.2 Modulus of elasticity of sleeper material

To quantify the effect of the interaction on the sleeper, we view the maximal strain within the sleeper during the load pattern. Strain is a quantity measuring how much an object is compressed or stretched.

The maximal strain over all sleeper elements for different moduli of elasticity of the sleeper material of $10^9, 10^{10}, 10^{11}$ and 10^{12} Pa is visualized in Figure 6.8. Due to the relation to the dilation radius a Young's modulus of at least 1 GPa is required. A reasonable modulus of elasticity for timber is 9 GPa and thus, the requirement due to the dilation radius does not restrict the physical properties of the sleeper.

First of all, we want to point out that a linear correlation between strain and Young's modulus is depicted. During the load pattern the strain increases in all curves by a factor of 200. Thus, the object experiences a deformation. However, the deformation is small which indicates that the sleeper is not impaired from the interaction.

6.4.3 Ballast size distribution

The results of varying the size distribution of the particle population is given in Figure 6.9 displaying the normal and piece-wise constant distribution as presented before. A notable difference is that the sleeper starts at different heights after the initial positioning. This is natural as we simulate with smaller particles in the piece-wise constant distribution, and thus the particles are sticking out much less. The amplitude of the sleeper movement during the cyclic loading pattern is more regular and smaller for the piece-wise constant distribution. That indicates that the ballast bed distributes the pressure more smoothly for smaller particles. It is reasonable that the signal is smoother for smaller particles, since the distance between the sensors and the sleeper is short.

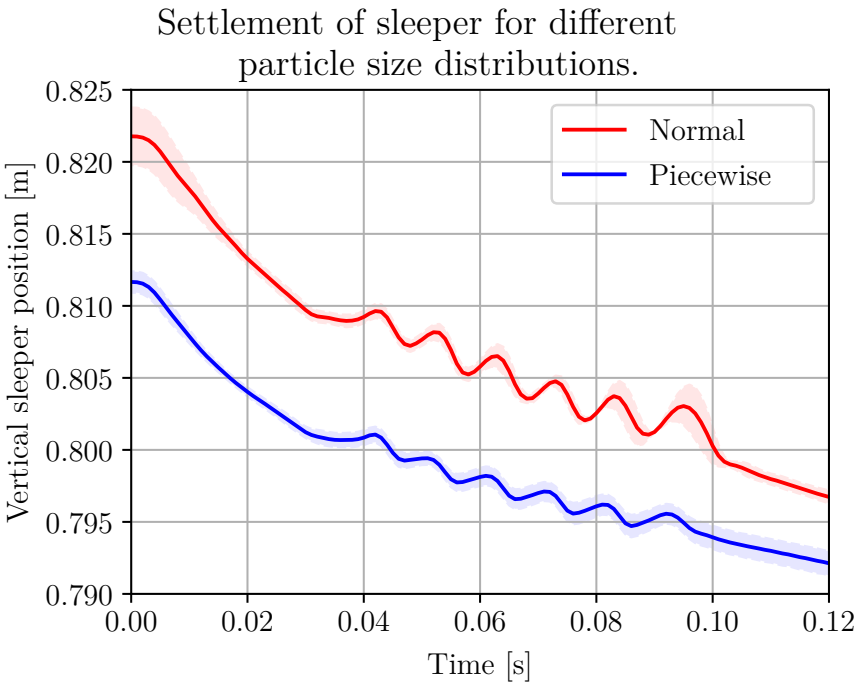

Figure 6.9: Vertical position of sleeper representing its settlement for normal and piece-wise constant distributed ballast sizes.

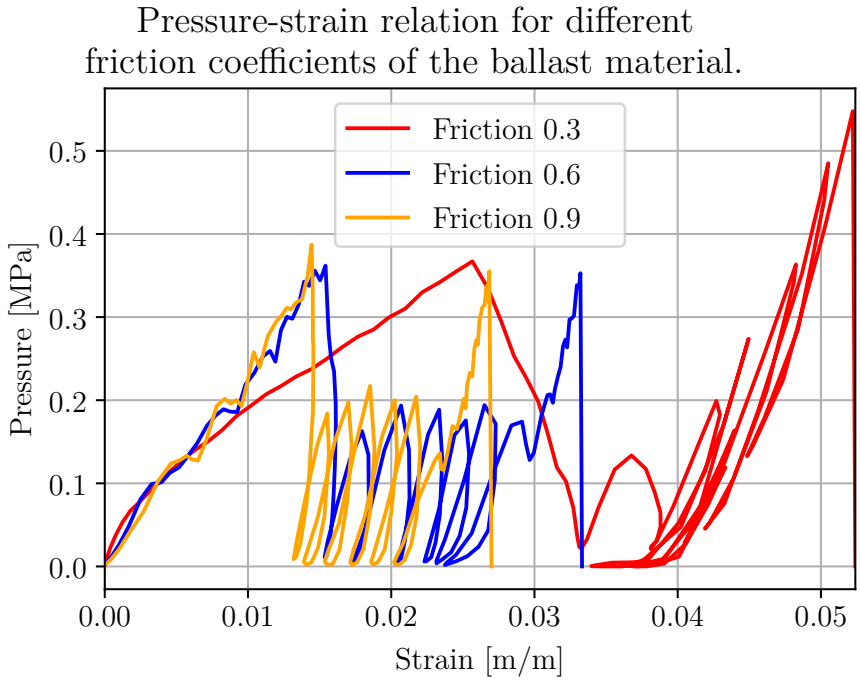

Figure 6.10: Pressure-strain relation for different friction coefficients of the ballast material.

6.4.4 Ballast friction coefficient

As the friction coefficient influences the interlocking ability of the ballast bed, we investigate the effect of changes in the friction coefficient.

In Figure 6.10 the strain derived from the sleeper settlement in relation to the pressure acting on the sleeper is given. We investigate the pressure-strain relation for frictions of $0.3, 0.6$ and 0.9.

It is striking that the results for a friction of 0.3 are unphysical. The pressure for this value is significantly higher than for the other values, leading to an increased strain.

For increasing friction values, the simulation seems to get more stable. Additionally, the maximal strain reduces for higher frictions. However, a friction of 0.9 is an untypical value for rock materials.

6.4.5 Modulus of elasticity of ballast material

As elaborated earlier in this chapter, the dilated polyhedron model requires a sufficiently high modulus of elasticity to avoid too large overlaps during contacts.

The settlement of the sleeper for varying the Young's modulus of the particle material is given in Figure 6.11. We consider a Young's modulus of 10 GPa, as well as half (5 GPa) and double (20 GPa) of it. However, no difference in the result is noticeable for the chosen values.

6.4.6 Particle resolution

Lastly, we investigate the particle resolution. As elaborated, we apply the dilated polyhedron model for *convex* particle geometry. Due to the convexity requirement on the particle models, higher resolution particles have less sharp nodes and smaller faces. Thus, the interaction is affected as well as the interlocking characteristics.

In Figure 6.12 the sleeper settlement for different particle resolutions with $10, 30$ and 40 triangles is shown. The settlement increases clearly from a resolution of 10 triangles to the higher resolutions. However, no significant difference is visible between 30 and 40 triangles. Additionally, we see similar effects as for a varying friction. The less triangles, the higher is the friction for convex particle models, which leads to less settlement in the particle bed.

With a smaller statistical variation, the results are also more stable for higher resolved particles, but again with no difference between 30 and 40 triangles. Hence, we conclude that a resolution of 30 triangles of the simulated rock particles is sufficient

6.5 Simulation results of pressure distribution at sensors within ballast bed

With the insights of the previous section, we choose to compare a simulation with a parameter choice that promises the best results to the experimental pressure dis-

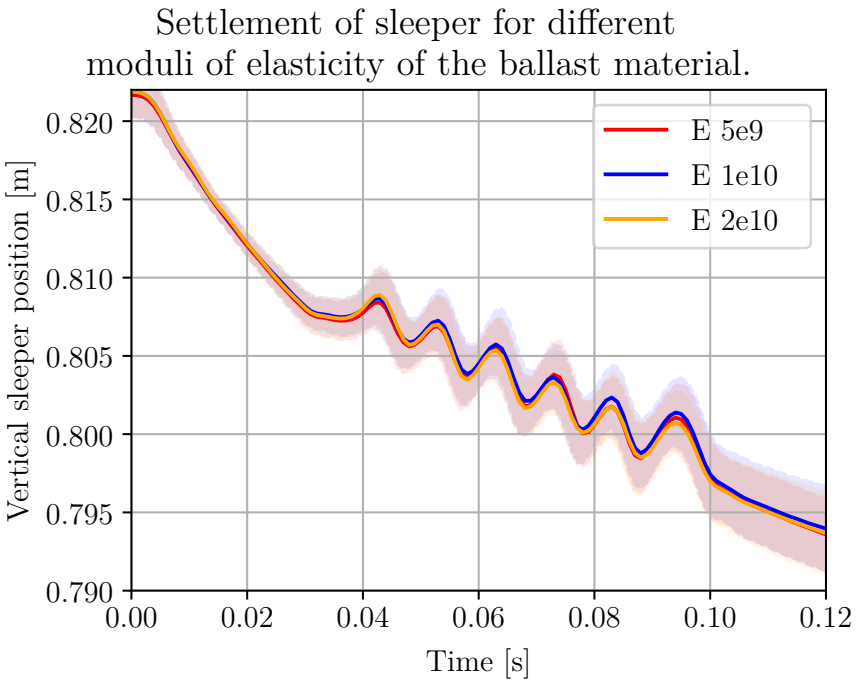

Figure 6.11: Vertical position of sleeper representing its settlement for different moduli of elasticity E.

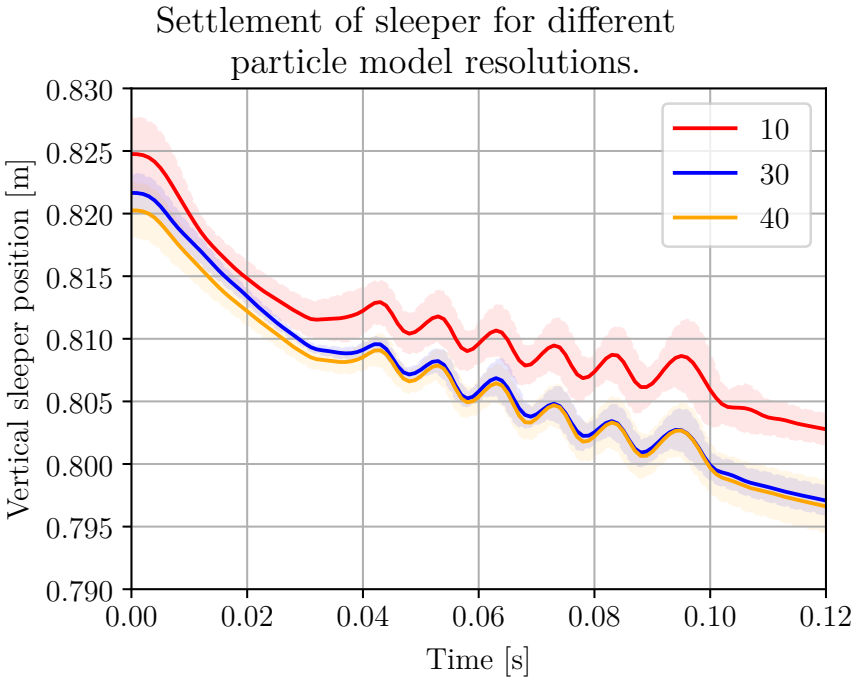

Figure 6.12: Vertical position of sleeper representing its settlement for different particle resolutions stated with the number of triangles in the particle geometry.

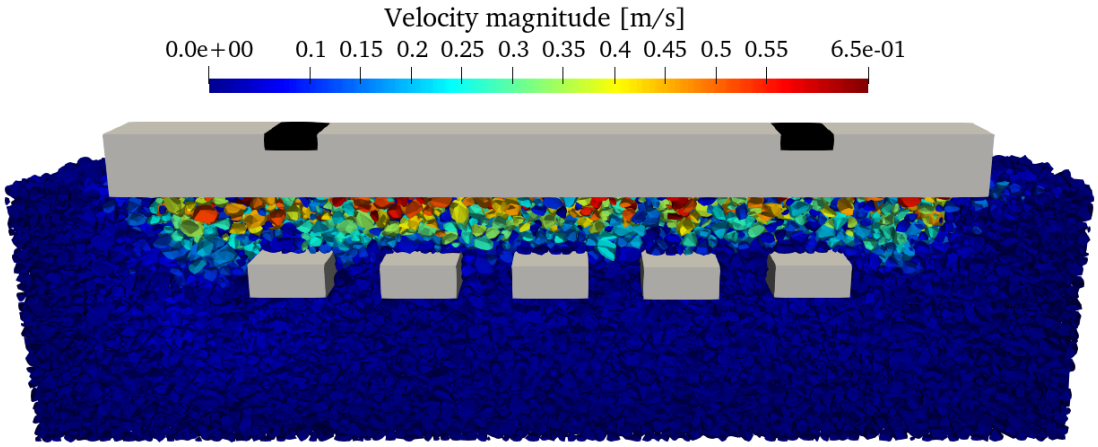

Figure 6.13: Simulation snapshot of the velocity distribution within a cross-section of the ballast bed for a load of 44 kN onto the rail positions (highlighted in black) on the sleeper.

tribution results given by Song et al. [31]. Thus, we simulate with a time scaling of 10.0, a friction of 0.6, a modulus of elasticity of 10^{10} for the particle and sleeper material, and a particle resolution of 30 triangles. Additionally, we choose to place the sensors at a depth of 0.26 m beneath the ballast bed surface. In the experiment they are positioned at a depth of 0.13 m, however in the corresponding simulation performed by Song et al. [31], the pressure distribution is recreated by computing the Cauchy stress tensor for a cuboid volume at the sensor position. As we only measure the pressure onto our sensors from the top, it could be higher than the actual measured or recreated one. Thus, we also investigated a lower sensor position that then measures the lower pressure distribution. For the lower positioned sensors we achieve results of a good quantitative match with the experiments, whereas for the original position, the measured pressure was higher for all five sensors.

A snapshot of the simulation with parameters stated above and the normal size distribution is given in Figure 6.13. At the time of the snapshot a load of 44 kN is applied onto the sleeper.

In Figure 6.14 the pressure distribution within the ballast bed given by the sensor measurements for both size distributions is visualized. The solid lines represent the experimental and the dashed ones our simulation results. As mentioned before, the pressure distribution was evaluated and shared at two loads before and after cyclic loading. The load of 44 kN is represented by triangles and 132 kN by circles. The result before cyclic loading are to the left and after cyclic loading to the right. Our results are clearly in the same quantitative range as the experimental results for both size distributions.

Let us first discuss the results for the normal size distribution in Figure 6.14a. It is visible, that some trends are represented by our data, e.g. the peak at the middle sensor for a load of 132 kN before and after cyclic loading. Our results for sensors 2 and 4 for that load are close to the experimental measurement. However, we did

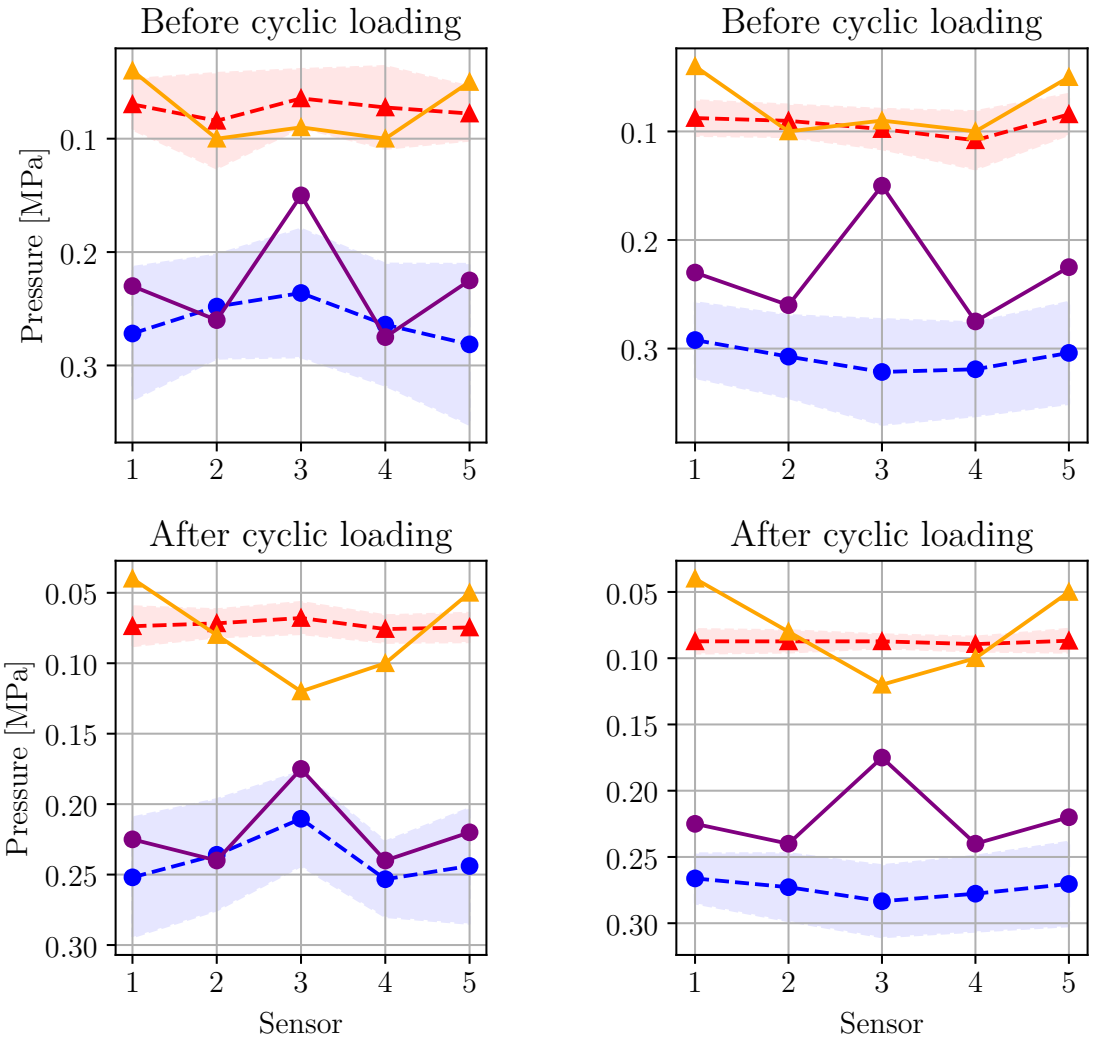

(a) Normal distribution **(b)** Piece-wise constant distribution

Figure 6.14: Comparison of pressure distribution in the sensors of experimental (solid) against simulation (dashed) results. The comparison is performed for two load levels, namely 44 kN (triangle markers) and 132 kN (circular markers), both before and after cyclic loading.

# Particles	Total time	DEM	FEM	Coupling
83,000	25	10 (40 %)	10 (40 %)	5 (20 %)
300,000	43	28 (67 %)	10 (22 %)	5 (11 %)

Table 6.2: Performance measurement in minutes of the total time of the coupling algorithm, separated in the pure DEM simulation, the pure FEM simulation and operations specific for the coupling. The results are given as the mean over 10 repetitions.

not match the curvature of the lower load of 44 kN and our measured distribution seems to be constant over the different sensors. That could be due to a too weak compaction of the particle bed. A too weak compaction could also cause the lower peak of sensor 3 for the higher load before cyclic loading. As we perform a compaction with a fixed amplitude, we might not compact as much as possible. How to perform a sufficient compaction could be a subject of a further study.

For the piece-wise constant distribution as presented in Figure 6.14b, the values for the lower load level are closer to the experimental data than for the normal distribution. However, similarly to the normal distribution, the pressure of the outer sensors is not matched. Also the pressure distribution for the higher load level is further away from the experimental data than for the normal distribution. Another observation is, that the pressure distribution for a higher load shows more symmetry in the pressure distribution and the statistical variation is smaller. We conclude that the simulated pressures are in a correct quantitative range, compared to experiments, and that further parameter calibration is required to obtain a spot-on approximation of the experimental data.

6.6 Performance measurements

In Table 6.2 we summarize computational performance results of the coupled sleeper-ballast simulations. The timing is split in the total simulation time, DEM and FEM simulation time and the total time of all the specific operations of the coupling algorithm. We measure the computation time for both distributions. For the normal distribution we simulate a total of 83,000 and for the piece-wise constant distribution 300,000 particles.

Similarly to the time measurements in section 5.6, the separate solvers account for an expected amount of the total time, as the number of degrees of freedom in DEM with 300,000 particles exceeds the number of degrees of freedom in FEM with 800 elements. The higher percentage of the coupling algorithm for the normal distribution is likely due to the fact that the coupling is performed with a smaller timestep in comparison to the solver timesteps than in the previous simulation case. However, the coupling algorithm still accounts for the least amount of time, which in itself is an important result as it shows that a sufficiently performant coupling algorithm has been implemented.

All simulations for the time measurement have been run on a machine with a Xeon Gold 6134 CPU with a clock speed of 3.20 GHz, 8 cores and 192 GB of memory as well as a V100 GPU with 32 GB of memory. Many simulations have been performed on other standard desktop machines with lower specification GPUs which also gave acceptable performance.

Note that both the solvers and the coupling algorithm are high performant which is an important aspect also for the scientific investigations. It enables us to do large repetitive studies to study important aspects such as the influence of the material and simulation parameters as well as the statistical variation within the simulation results. In particular, the latter is often overlooked due to low computational performance of the solvers. In particular the utilization of the GPU in the DEM solver allows for extreme simulation capacity also with a standard desktop with a single GPU.

7

Conclusion

Within this thesis we implemented a high performant coupling algorithm combining the FCC in-house solvers Demify® and LaStFEM. The implementation was purely based on Python using the solver interfaces and no alteration of the solvers themselves was required. The coupled solver allows for simulation of the interaction between particle systems and elastic bodies.

With the elastostatic case of a fixed beam under uniformly distributed constant load we verified the correct data transfer of contact forces from DEM to FEM. In comparison to the FEM solution, we achieved a relative error to the finite element solution of less than 1 % for a load of 51 kg.

The surface coupling was applied to the simulation case of a steel sheet under material flow. With that we showed that the coupling framework is applicable for elastodynamics. Additionally, we compared our simulation results to experimental measurements of the sheet deflection with good agreement.

Following the primary goal of this thesis, we applied the DEM-FEM coupling for the simulation of railroad ballast. Specifically, we simulated the interaction of the sleeper with the ballast bed under load. By introducing the predictive coupling, we optimized the stability of the coupled solution. The adapted scheme allows for a 10 times higher coupling timestep than for the just-in-time coupling.

Furthermore, we performed parameter studies to investigate the effect of varying properties on the interaction and with that also the simulation results. We found that significant parameters with noticeable effect on the simulation outcome are the particle size distribution, friction coefficient of the ballast material, particle model resolution and the acceleration of the load pattern applied on the sleeper. The results of the comparison against experimental data for the pressure distribution within the ballast bed demonstrate good qualitative and quantitative agreement.

Concerning the computational performance of the coupled solution, we were able to simulate a wide range of parameters repetitively, which represents an important property for a digital framework. The coupling can be performed on a standard desktop with a single GPU.

7.1 Research questions

- *How to develop a DEM-FEM coupling matching the current state-of-art in the open literature?*

  We developed a high performant DEM-FEM surface coupling algorithm based on existing state-of-art DEM and FEM solvers. The implementation is in relation to the current state-of-art open literature.

- *How is a stable and convergent scheme between the solvers formulated and implemented?*

  Sufficiently small timesteps to resolve the physical equations in DEM and FEM are required. As we emphasized, parameter studies are a basis for calibration and ensuring stable numerics. The calibration of the model parameters is necessary to approximate experimental results and was successfully performed in the case of a steel sheet in chapter 5.

- *What are the temporal and spatial resolutions required to achieve convergent solutions?*

  For systems with high forces, relatively short timesteps are required in order to have a stable simulation method. However, the here presented coupled solution allows for a timestep 10,000 times larger than in the simulations performed by Song et al. [31] for the interaction between sleeper and ballast bed.

- *What are the required algorithms to get sufficient performance in the coupling?*

  The performance measurements of the coupled solution showed that the computational time of the coupling specific operations are significantly lower in comparison to the cost of the DEM and FEM solver. As elaborated earlier, this is an expected result as the operations performed by the coupling are small and do not require the solution of a system of equations. Thus, the measurements show that the coupling algorithm is implemented in an efficient way.

  To be more specific, for a number 86,000 particles and 340 quadrilateral elements of the object discretization, the total computation time was 116 minutes for a total simulated time of 5.0 s. This allows for the coupling algorithm to be applied on standard desktop computer systems and for wide parameter studies as well as studies of statistical variation.

- *What questions concerning railroad ballast simulations with DEM-FEM couplings are not answered yet by the current state-of-art?*

  We showed that with simulations of complex-shaped particles we can approximate the results of laboratory experiments. Furthermore, the implementation of the coupled solution is high performant.

- *Can the influence of the shape of the particle be quantitatively characterized to show the importance for ballast simulations and railroad construction?*

  We tested simulations with the dilated polyhedron particle model for convex particle geometries. The scope of this thesis did not allow for further comparison to other particle representations.

7.2 Future work

Aspects for possible future work on the coupling framework are:

- A more detailed investigation on the improvement in stability with the predictive coupling. We already saw that it allowed for a larger timestep as compared to the just-in-time coupling. Further interesting aspects are to investigate if numerical damping is still required for stable simulations.
- Develop the coupling algorithm further to allow more than one object in the FEM domain. This could be especially interesting for further infrastructure simulations where the subground below the ballast bed could be modelled with FEM.
- A comparison of varying particle representations such as dilated polyhedra, spheres, polyhedra and multi-spheres. For instance, the simulation of steel sheet under material flow with actually wheat-grain-shaped particles instead of spheres.

Aspects for future work concerning the simulation of railroad with a DEM-FEM coupling are:

- Particle breakage is a known phenomenon within ballast beds. The incorporation of a particle breakage model into the DEM simulation would allow the investigation of a different set of questions concerning the effects on the ballast bed.
- Large-scale simulations: The inclusion of the modelling of rails on top of the sleeper, larger railroad sections with several sleepers connected by rails, varying ballast bed shapes, reparation of railroad, etc. The list of interesting simulation cases continuing on the simulation of railroad systems is large.
- Experimental studies providing several measurements and calibration quantities for railroad simulation together with simulations of those.

The work presented within this thesis will be continued in the Vinnova InfraSweden2030 project DigiRail, with its project lead at FCC. In DigiRail, the high-performance computing of construction, operation and maintenance of railroad infrastructure will be investigated.

Bibliography

[1] Tågoperatörerna. *Järnväg 2050 En vision om järnvägens framtida roll i samhället.* 2019. URL: https://www.almega.se/app/uploads/sites/9/2019/11/bto-jarnvag2050.pdf (visited on 03/29/2022).

[2] Trafikverket. *Underhåll av väg och järnväg.* 2021. URL: https://www.trafikverket.se/resa-och-trafik/underhall-av-vag-och-jarnvag/ (visited on 03/29/2022).

[3] Naturvårdsverket. *Inrikes transporter, utsläpp av växthusgaser.* URL: https://www.naturvardsverket.se/data-och-statistik/klimat/vaxthusgaser-utslapp-fran-inrikes-transporter/ (visited on 05/04/2022).

[4] Yahia Alabbasi and Mohammed Hussein. "Geomechanical Modelling of Railroad Ballast: A Review". In: *Archives of Computational Methods in Engineering* 28.3 (Dec. 2019), pp. 815–839.

[5] Mingfei Lu and Glenn R. McDowell. "Discrete element modelling of railway ballast under triaxial conditions". In: *Geomechanics and Geoengineering* 3.4 (2008), pp. 257–270.

[6] Buddhima Indraratna, D Ionescu, and HD Christie. "Shear behavior of railway ballast based on large-scale triaxial tests". In: *Journal of geotechnical and geoenvironmental Engineering* 124.5 (1998), pp. 439–449.

[7] Andrew K. Rohrman, Hamed F. Kashani, and Carlton L. Ho. "Effects of natural abrasion on railroad ballast strength and deformation properties". In: *Construction and Building Materials* 247.118315 (2020).

[8] Xu Zhang et al. "Investigation of track settlement and ballast degradation in the high-speed railway using a full-scale laboratory test". In: *International Journal of Geomechanics* 233.8 (Dec. 2018), pp. 869–881.

[9] B. Aursudkij, G. R. McDowell, and A. C. Collop. "Cyclic loading of railway ballast under triaxial conditions and in a railway test facility". In: *Granular Matter* 11.6 (May 2009), pp. 391–401.

[10] Jan Stransky. "Open Source DEM-FEM Coupling". In: *Particle-Based Methods III: Fundamentals and Applications.* Ed. by Bischoff, M and Ramm, E and Onate, E and Owen, R and Wriggers, P. 3rd International Conference on Particle-based Methods, Stuttgart, Germany, SEP 18-20, 2013. Univ Stuttgart; Univ Hannover; Swansea Univ; European Community Computat Methods Appl Sci Secretariat; CIMNE; Int Assoc Computat Mech. 2013, 46–57.

[11] Zheng Lu et al. "Particle impact dampers: Past, present, and future". In: *Structural Control and Health Monitoring* 25.1 (June 2017), e2058.

[12] Mark Michael, Frank Vogel, and Bernhard Peters. “DEM-FEM coupling simulations of the interactions between a tire tread and granular terrain”. In: *Computer Methods in Applied Mechanics and Engineering* 289 (2015), pp. 227–248.

[13] H Nakashima and A Oida. “Algorithm and implementation of soil–tire contact analysis code based on dynamic FE–DE method”. In: *Journal of Terramechanics* 41.2 (2004). 14th International Conference of the ISTVS, pp. 127–137.

[14] Haiyang Zeng et al. “Calibration and validation of DEM-FEM model parameters using upscaled particles based on physical experiments and simulations”. In: *Advanced Powder Technology* 31.9 (Sept. 2020), pp. 3947–3959.

[15] Q.J. Zheng et al. “A coupled FEM/DEM model for pipe conveyor systems: Analysis of the contact forces on belt”. In: *Powder Technology* 314 (June 2017), pp. 480–489.

[16] Shaomin Liang and Shunying Ji. “DEM-FEM Coupling Analysis of Safe Landing of Reentry Capsule Considering Landing Attitude and Rebound Response”. In: *Journal of Aerospace Engineering* 34.4 (2021).

[17] YC Chung et al. “Mechanical behaviour of a granular solid and its contacting deformable structure under uni-axial compression – Part I: joint DEM–FEM modelling and experimental validation”. In: *Chemical Engineering Science* 144 (2016), pp. 404–420.

[18] Fubin Tu et al. “A sequential DEM-FEM coupling method for shot peening simulation”. In: *Surface and Coatings Technology* 319 (June 2017), pp. 200–212.

[19] Song Liming et al. “Research on mining truck vibration control based on particle damping”. In: *IOP Conference Series: Materials Science and Engineering*. Vol. 324. 012011. IOP Publishing. 2018.

[20] Huanran Wu, Jidong Zhao, and Ning Guo. “Multiscale Insights Into Borehole Instabilities in High-Porosity Sandstones”. In: *Journal of Geophysical Research: Solid Earth* 123.5 (May 2018), pp. 3450–3473.

[21] Alon Mazor et al. “A combined DEM & FEM approach for modelling roll compaction process”. In: *Powder Technology* 337 (Sept. 2018), pp. 3–16.

[22] Wei Wang et al. “Using FEM-DEM coupling method to study three-body friction behavior”. In: *Wear* 318.1-2 (2014), pp. 114–123.

[23] Eugenio Onate et al. “Advances in the DEM and Coupled DEM and FEM Techniques in Non Linear Solid Mechanics”. In: *Advances in computational plasticity*. Ed. by Onate, E and Peric, D and Neto, ED and Chiumenti, M. Vol. 46. Computational Methods in Applied Sciences. 14th International Conference on Computational Plasticity, Fundamentals and Applications (COMPLAS), Barcelona, Spain, Sep 05-07, 2017. 2018, pp. 309–335.

[24] Jaap Meijaard. “Lateral impacts on flexible beams in multibody dynamics simulations”. In: *IUTAM Symposium on Multiscale Problems in Multibody System Contacts*. Ed. by Eberhard, P. Vol. 1. IUTAM Bookseries. IUTAM Symposium on Multiscale Problems in Multibody System Contacts, Stuttgart, Germany, Feb 20-23, 2006. IUTAM. 2007, pp. 173–182.

[25] Wen-Jie Xu and Yang Zhao. “A Coupling Finite-Discrete Element Method for Mechanical Analysis of Granular Materials”. In: *GeoShanghai International Conference*. Springer. 2018, pp. 901–910.

[26] Mathias Dratt and André Katterfeld. “Coupling of FEM and DEM simulations to consider dynamic deformations under particle load”. In: *Granular Matter* 19.3 (June 2017).

[27] Mykola Sysyn et al. “Mechanism of Sleeper–Ballast Dynamic Impact and Residual Settlements Accumulation in Zones with Unsupported Sleepers”. In: *Sustainability* 13.14 (July 2021), p. 7740.

[28] Guoqing Jing et al. “Micro-analysis of hanging sleeper dynamic interactions with ballast bed”. In: *Journal of Vibroengineering* 17.1 (2015), pp. 444–454.

[29] S Kaewunruen and O Mirza. “Hybrid Discrete Element - Finite Element Simulation for Railway Bridge-Track Interaction”. In: *IOP Conference Series: Materials Science and Engineering* 251.012016 (Oct. 2017).

[30] Xuejun Wang et al. “Modeling of Coupling Mechanism between Ballast Bed and Track Structure of High-Speed Railway”. In: *Mathematical Problems in Engineering* 2020 (Feb. 2020), pp. 1–12.

[31] Weimin Song et al. “Interaction between Railroad Ballast and Sleeper: A DEM-FEM Approach”. In: *International Journal of Geomechanics* 19.04019030 (May 2019).

[32] Yohei Koike et al. “Numerical method for evaluating the lateral resistance of sleepers in ballasted tracks”. In: *Soils and Foundations* 54.3 (June 2014), pp. 502–514.

[33] J. Quist, F Hunger, and K Jareteg. *Segregation of rock materials during unloading.* Tech. rep. Fraunhofer-Chalmers Centre for Industrial Mathematics, Computational Engineering & Design. Gothenburg, 2019.

[34] J. Quist et al. *Investigation of the effect of size segregation on roller compaction of unbound materials.* Tech. rep. Fraunhofer-Chalmers Centre for Industrial Mathematics, Computational Engineering & Design. Gothenburg, 2021.

[35] P. A. Cundall and O. D. L. Strack. “A discrete numerical model for granular assemblies”. In: *Géotechnique* 29.1 (1979), pp. 47–65.

[36] H. P. Zhu et al. “Discrete particle simulation of particulate systems: Theoretical developments”. In: *Chemical Engineering Science* 62.13 (2007). Frontier of Chemical Engineering - Multi-scale Bridge between Reductionism and Holism, pp. 3378–3396.

[37] Da Wang. “Accelerated granular matter simulation”. PhD thesis. Umeå University, 2015.

[38] Kasra Samiei et al. “Assessment of the potentials of implicit integration method in discrete element modelling of granular matter”. In: *Computers & chemical engineering* 49 (2013), pp. 183–193.

[39] Ben Nye, Anton V Kulchitsky, and Jerome B Johnson. “Intersecting dilated convex polyhedra method for modeling complex particles in discrete element method”. In: *International journal for numerical and analytical methods in geomechanics* 38.9 (2014), pp. 978–990.

[40] Cheng-Qing Li, Wen-Jie Xu, and Qing-Shan Meng. “Multi-sphere approximation of real particles for DEM simulation based on a modified greedy heuristic algorithm”. In: *Powder Technology* 286 (2015), pp. 478–487.

[41] Adam Bilock. *A GPU Polyhedral Discrete Element Method.* 2020.

[42] Shunying Ji, Shanshan Sun, and Ying Yan. “Discrete element modeling of rock materials with dilated polyhedral elements”. In: *Procedia engineering* 102 (2015), pp. 1793–1802.

[43] S Ji, S Sun, and Y Yan. “Discrete element modeling of dynamic behaviors of railway ballast under cyclic loading with dilated polyhedra”. In: *International Journal for Numerical and Analytical Methods in Geomechanics* 41.2 (2017), pp. 180–197.

[44] Colin Thornton, Sharen J Cummins, and Paul W Cleary. “An investigation of the comparative behaviour of alternative contact force models during inelastic collisions”. In: *Powder technology* 233 (2013), pp. 30–46.

[45] Heinrich Hertz. “On the contact of elastic solids”. In: *Z. Reine Angew. Mathematik* 92 (1881), pp. 156–171.

[46] Colin Thornton, Sharen J Cummins, and Paul W Cleary. “An investigation of the comparative behaviour of alternative contact force models during elastic collisions”. In: *Powder Technology* 210.3 (2011), pp. 189–197.

[47] Raymond David Mindlin. *Compliance of elastic bodies in contact*. 1949.

[48] Hamzah M Beakawi Al-Hashemi and Omar S Baghabra Al-Amoudi. “A review on the angle of repose of granular materials”. In: *Powder technology* 330 (2018), pp. 397–417.

[49] Michele Marigo and Edmund Hugh Stitt. “Discrete Element Method (DEM) for Industrial Applications: Comments on Calibration and Validation for the Modelling of Cylindrical Pellets”. In: *KONA Powder and Particle Journal* 32 (2015), pp. 236–252.

[50] M Jon Turner et al. “Stiffness and deflection analysis of complex structures”. In: *journal of the Aeronautical Sciences* 23.9 (1956), pp. 805–823.

[51] Ted Belytschko et al. *Nonlinear finite elements for continua and structures*. John Wiley & Sons, 2014.

[52] Niels Saabye Ottosen and Hans Petterson. “Introduction to Finite Element Method”. In: *Prentice Hall Europe* 1 (1992).

[53] Thomas JR Hughes. *The finite element method: linear static and dynamic finite element analysis*. Courier Corporation, 2012.

[54] WL Wood, M Bossak, and OC Zienkiewicz. “An alpha modification of Newmark’s method”. In: *International journal for numerical methods in engineering* 15.10 (1980), pp. 1562–1566.

[55] Richard Gordon Budynas, J Keith Nisbett, et al. *Shigley’s mechanical engineering design*. 9th ed. Vol. 9. McGraw-Hill New York, 2011.